



A novel framework for combining polarimetric Sentinel-1 InSAR time series in subsidence monitoring - A case study of Sydney

Alex Hay-Man Ng^{a,b,d}, Ziyue Liu^a, Zheyuan Du^{c,d,*}, Hengwei Huang^a, Hua Wang^e, Linlin Ge^d

^a Department of Surveying Engineering, Guangdong University of Technology, Guangzhou, China

^b Key Laboratory for City Cluster Environmental Safety and Green Development of the Ministry of Education, Guangdong University of Technology, Guangzhou, China

^c Geoscience Australia, Canberra, Australia

^d School of Civil and Environmental Engineering, University of New South Wales (UNSW), Sydney, NSW 2052, Australia

^e College of Natural Resources and Environment, South China Agricultural University, Guangzhou, China

ARTICLE INFO

Edited by Jing M. Chen

Keywords:

InSAR
Sydney subsidence
Polarimetric time-series InSAR
Deformation mapping
Tunnel subsidence

ABSTRACT

The rapid growth of the city of Sydney, Australia over the last decades, has led to significant development of residential and transportation infrastructure. Land subsidence associated with the urban development can lead to serious issues which should be thoroughly understood and carefully managed. To address this challenge, an enhanced polarisation time-series InSAR (Pol-TS-InSAR) processing framework was developed, using the dual polarisation (DP) Sentinel-1 data to integrate information from different polarimetric channels with different weighting during the TS-InSAR deformation analysis. Ninety DP Sentinel-1 images acquired between 2019 and 2022 are analysed using Pol-TS-InSAR to map the land subsidence in Sydney, with the assistance of the GPS measurements. Improvement of measurement points density from Pol-TS-InSAR is observed compared to the single polarimetric TS-InSAR counterpart for all land use types (ranging between 68% and 208%). The comparison between the Pol-TS-InSAR measurements and GPS measurements shows an absolute mean difference and RMS difference of 0.75 mm/yr and 0.95 mm/yr, respectively, in vertical direction. The results of the ground subsidence analysis revealed that the main subsidence factors in Sydney are related to groundwater extraction, mining activities, underground tunnel construction and landfill. The latter two factors were less well-known prior to this study. In addition to these factors, land subsidence related to high-rise building construction has also been observed, even though the impact seems to be less significant than other factors.

1. Introduction

Land subsidence is a globally challenging problem that affects more than 50 countries and can lead to serious social, economic and environmental problems (Herrera-García et al., 2021). Groundwater extraction, high-rise building construction, and underground tunnel excavation are some of the typical factors for land subsidence in urban areas. Sydney, the capital city of the state of New South Wales, is one of the most populous cities in both Australia and Oceania. Land subsidence in Sydney can cause significant economic loss, particularly in urban areas and can even pose a threat to human life if not properly understood and managed. Previous studies suggested that Sydney was relatively stable (Ng et al., 2011) where the main causes of land deformation is possibly groundwater extraction (Ng et al., 2008) and urban development (Stewart, 2019). Bateman et al. (2020) later conducted a study on

monitoring the land subsidence due to the construction of the Sydney Metro Northwest tunnel using Envisat and TerraSAR-X SAR imagery and suggested that the ground deformation from tunnelling could be considered as negligible due to Sydney's geology. Despite this, the city of Sydney has been growing rapidly in recent years, particularly since the commencement of the WestConnex project, Australia's largest road infrastructure project, in 2015. Since 2019, the construction of the last stage of the WestConnex project, a 7.5 km underground tunnel across the metropolitan area in Sydney, has been underway. The construction of underground tunnels can trigger ground subsidence, making monitoring the excavation induced deformation necessary during and after construction to prevent potential risks to economic resources and human safety. In addition to the transportation construction, the rapid expansion of urban boundaries in recent years is also prone to land subsidence. Therefore, understanding the subsidence phenomenon in the city is

* Corresponding author at: Geoscience Australia, Canberra, Australia.

E-mail address: z.du@unsw.edu.au (Z. Du).

<https://doi.org/10.1016/j.rse.2023.113694>

Received 12 October 2022; Received in revised form 10 May 2023; Accepted 17 June 2023

0034-4257/© 2023 The Authors. Published by Elsevier Inc. This is an open access article under the CC BY-NC license (<http://creativecommons.org/licenses/by-nc/4.0/>).

important for effective geohazard management.

Satellite Synthetic Aperture Radar (SAR) interferometry is well-established for regional land deformation mapping due to its large coverage, high resolution and high accuracy (Dzurisin, 2007; Ferretti et al., 2001). Time-series SAR interferometry (TS-InSAR), utilising stacking of SAR time-series imagery, has been operationally used for monitoring long-term land stability, particularly in areas with InSAR favourable conditions (e.g. infrastructure, desert, or area with sparse vegetation and a dry climate) (Liu et al., 2023; Onuma and Ohkawa, 2009; Rucci et al., 2012; Zhang et al., 2016). The conventional TS-InSAR methods were developed for SAR images acquired at a single polarimetric channel. In recent years, new generation satellite SAR sensors such as Sentinel-1 (S1) and ALOS-2 are able to provide polarimetric data for operational use. Since different polarimetric channels are sensitive to different geometric characteristics of ground features, the availability of new generation SAR sensors has provided the opportunity to exploit the polarimetric SAR data to improve the performance for deformation monitoring applications (i.e. accuracy and density of the measurement points).

The concept of Polarimetric SAR Interferometry (Pol-InSAR) was first introduced by Cloude and Papathanassiou (1998). One of the earliest TS-InSAR studies to use multi-polarisation SAR data was conducted by Pipia et al. (2009). Navarro-Sanchez et al. (2014; 2010) developed a general polarimetric optimisation method, building on Pipia et al. (2009)'s work, and applied it to optimize both the amplitude dispersion index (ADI) and the coherence stability index. These methods were used to assess the performance of Pol-TS-InSAR analysis using the full-polarisation (FP) data, and the results show that a significant increase in measurement point (MP) by up to 310% has been observed in comparison to the single-polarisation (SP) data. Ishitsuka et al. (2014) proposed a method to incorporate the dual-polarisation (DP) SAR data (co-pol HH and VV data) for TS-InSAR analysis, showing that the MP can be increased by 48–70% compared with the single-pol results. However, the lack of cross-pol (HV and VH) can limit the ability to synthesise the full-pol space. Esmaeili et al. (2017) introduces a polarimetric form of amplitude difference dispersion (ADD) criterion for small baseline analysis with full-resolution interferograms. Sadeghi et al. (2018) presented a Pol-TS-InSAR method based on polarimetric optimisation of temporal coherence to identify the scatterers with stable phase characteristics. They implemented the polarimetric optimisation on Standford Method for PS (StaMPS) and applied it to the DP (co-pol) TSX data.

Although most of the Pol-TS-InSAR studies employed either the full-pol or co-pol SAR data, several studies have investigated effective ways to utilise the polarimetric information for TS-InSAR with the cross-pol data (Azadnejad et al., 2019, 2020; Ishitsuka et al., 2017; Shamshiri et al., 2018). Ishitsuka et al. (2017) proposed an approach to optimize the polarimetric information based on the weighting method. They examined the optimised approach using full polarimetric ALOS-1 PAL-SAR data, and found that it increased the number of MP point by approximately 80–280% and 10% for full-pol and cross-pol data, respectively, compared to single polarimetric approaches. Shamshiri et al. (2018) and Azadnejad et al. (2019, 2020) investigated the potential of DP S1 (VV/VH) for improving the polarimetric optimisation results. The results showed an overall increase of approximately 70% - 186% in the number of MP points for S1 data, at different test sites. Shen et al. (2022) in a recent study proposed the PSC selection and interferogram phase optimisation methods based on Trace Moment based statistical properties and Total Power Interferogram Construction. Shen et al. showed that the proposed method can improve the deformation detection performance better than the polarimetric optimisation methods based on ADI, in terms of the quality of interferometric phase, density of PSs, and computation efficiency. Zhao et al. (2022) suggested that Pol-TS-InSAR with the adaptive optimisation strategies can further improve its performance for applications in rural area but at the price of highest computation cost. It is worth noting that most of these Pol-TS-

InSAR studies have focused on integrating the multi-polarisation data at the PSC Selection and Interferogram Generation stages, which little attention paid to the later stage of the TS-InSAR process. The main advantage of integrating the multi-polarisation data in the preliminary stage of TS-InSAR is to reduce the required computation resources and to save the development time. This works well in many cases, but there are cases that the phase information from different polarisation channels is not fully utilised, which will be discussed later in the manuscript.

This study builds upon the foundation of previous studies to investigate the feasibility of improving the performance of Pol-TS-InSAR, addressing to the shortcomings mentioned above. The study aims to achieve two objectives: (1) developing an enhanced TS-InSAR processing framework that further utilises the information from multi-polarisation channels, along with the polarimetric optimised channel, for improving the performance of PSI applications; (2) applying the developed processing framework for mapping the land deformation in Sydney, Australia using the dual polarisation Sentinel-1 data.

2. Methodology

2.1. Selection of persistent Scatterer with multi-polarisation channel

The Exhaustive Search Polarimetric Optimisation (ESPO) approach, a widely used approach for Polarimetric PS point optimisation, is employed in this work for PS point selection (Navarro-Sanchez et al., 2014; Navarro-Sanchez et al., 2010). For each resolution cell in the SAR image, fully polarimetric radar data, assuming reciprocity, can be represented by the reduced scattering vector k , i.e., (Cloude and Papathanassiou, 1998)

$$k = \frac{1}{\sqrt{2}}[S_{HH} + S_{VV}, S_{VV} - S_{HH}, 2S_{HV}]^T \quad (1)$$

where T denotes the transposition, and S_{ij} is the complex scattering coefficient for i transmitted and j received polarisation in the H (horizontal)-V (vertical) polarimetric basis. A scattering coefficient $\mu = \omega^* k$ can be defined by projecting the scattering vector k onto a complex unitary vector ω , where $*$ represents conjugated transpose (Cloude and Papathanassiou, 1998). The scattering coefficient μ , a linear combination of the elements of k , is equivalent to the complex value from a single-channel SAR system for a resolution cell (Navarro-Sanchez et al., 2014). This equivalence enables the time-series interferometry techniques developed for single-polarisation channel data to multi-polarisation channel data by applying them to μ . The general form of ω is given by (Navarro-Sanchez et al., 2010)

$$\omega = [\cos(\alpha), \sin(\alpha)\cos(\beta)e^{i\delta}, \sin(\alpha)\sin(\beta)e^{i\epsilon}]^T \quad (2)$$

where the values of the four parameters α , β , δ and ϵ , with finite ranges, are related to the geometric and electromagnetic features of the target (Cloude, 2010). Both α and β range from 0 to $\pi/2$ while δ and ϵ range from $-\pi$ to π .

In the case of DP S1 configuration, i.e. VV/VH, k can be defined as (Azadnejad et al., 2019, 2020; Shamshiri et al., 2018):

$$k = \frac{1}{\sqrt{2}}[S_{VV}, 2S_{VH}]^T \quad (3)$$

and the projection vector ω can be expressed as (Azadnejad et al., 2020; Navarro-Sanchez et al., 2014)

$$\omega = [\cos(\alpha), \sin(\alpha)\cos(\beta)e^{i\delta}]^T \quad (4)$$

where α and δ represents the type of scattering mechanism and the orientation of the target scatterer, respectively (Cloude, 2010). The α ranges from 0 (vertical dipole scattering) to $\pi/2$ (volumetric scattering) while δ ranges from $-\pi$ to π .

PS points are the coherent radar targets exhibiting high phase stability over a long period of time. These targets often correspond to the point-wise scatterers with odd-bounce or even-bounce scattering mechanisms, such as man-made structures, boulders, and tree trunks (Perissin and Ferretti, 2007). In the case of single polarisation channel data, the amplitude dispersion criterion is commonly used to select the persistent scatterer candidates (PSC). Let s be the complex scattering coefficient vector: $s(P) = [s_1(P), s_2(P), \dots, s_N(P)]^T$ where P is an image pixel and $s_i(P)$ is the scattering coefficient of the i th image of the image stack (with N images) corresponding to Pixel P . The amplitude dispersion criterion can be expressed as: $D_A = \sigma_s / \bar{s}$ where σ_s and \bar{s} is the standard deviation and the mean of the amplitude value of each element in $s(P)$, respectively.

For the polarimetric case, the number of quality of the PS point can be improved by using ESPO. This can be done by substituting the single-pol scattering coefficient s by the optimised scattering coefficient μ with the minimal amplitude dispersion index D_A^{pol} (Navarro-Sanchez et al., 2014). By constraining the same optimum ω for each pixel along all images within the image stack to avoid the introduction of variable phase term, D_A^{pol} can be expressed as

$$D_A^{pol} = \frac{1}{|\bar{s}| \sqrt{N}} \sqrt{\sum_{i=1}^N (|s_i| - |\bar{s}|)^2} \approx \frac{1}{|\bar{\omega}^* k| \sqrt{N}} \sqrt{\sum_{i=1}^N (|\omega^* k_i| - |\bar{\omega}^* k|)^2} \quad (5)$$

where N is the total number of SAR images in the image stack, and the overline indicates the mean. For the conventional method, pixels with D_A under a defined threshold will be selected as PSCs since low D_A indicates low amplitude dispersion along the image stack. The main idea of the ESPO is to search the N -dimensional space (i.e. α and δ for DP S1 configuration) to find the optimum projection vector ω that minimises D_A^{pol} . In this study, a conventional fine grid search with a step size of 0.05 rad is employed to find the solution of the two unknown parameters α and δ (for DP S1 configuration) that minimise the objective Eq. (5) at each pixel.

2.2. Weighted sum based joint multi-polarisation channels for model parameters estimation (WS-MPMP)

Ideally, the coherence of the interferometric phase obtained from the polarimetric PS point optimisation approach, like ESPO, is expected to be optimised (Cloude and Papathanassiou, 1998; Navarro-Sanchez et al., 2010). As a result, the polarimetric PS point optimisation approach can be conducted during the PSC selection stage to derive the optimised interferometric phase. This optimised data can then be directly processed using the conventional TS-InSAR framework to obtain the deformation parameters. This allows the maximal utilisation of the existing TS-InSAR software.

However, it is worth to note that conventional polarimetric stable scatterer optimisation approaches, such as ESPO, primary focused on optimising the two stable measurement point (MP) selection criteria, i.e. ADI or the average coherences (Navarro-Sanchez et al., 2014). These stable point selection criteria are often employed as an a-priori index of the stability of the MP candidate (MPC) selected for general TS-InSAR analysis. Ideally, higher quality stable point candidates can be expected when minimizing the ADI or maximizing the average interferometric coherences from multiple polarimetric channels compared to a single channel. By enhancing the quality of MPC, denser MP can be anticipated from the final deformation measurement results.

Nonetheless, Shen et al. (2022) demonstrated that the non-PS portion has significantly increased from the PSC chosen with the ESPO method, as discriminating between PS and non-PS from ESPO is challenging. One possible reason for this is that maximizing the quality of MPC according to ADI or the average coherence do not guarantee optimization of the estimated deformation parameters. To investigate this issue, an experiment was conducted over the study area of this work

(see Appendix A in supplementary document) to compare the temporal coherence (also known as ensemble phase coherence (Ferretti et al., 2001)) obtained by different polarisation channels (including the polarimetric optimised channel from ESPO) over the study area of this study. In TS-InSAR analysis, temporal coherence is often used as an a-posteriori index of the stable scatterer's behaviour of a point target (Colesanti et al., 2003), which can be expressed as:

$$\gamma_{x,y} = \left| \frac{\sum_{i=1}^N \exp(j\Delta\varphi_{x,y}^i - j\Delta\varphi_{Model,x,y}^i)}{N} \right| \quad (6)$$

where, $\Delta\varphi_{x,y}^i$ and $\Delta\varphi_{Model,x,y}^i$ is the observation phase and the model phase derived from the model parameters (i.e. DEM error and deformation rate) between pixel x and y . The results in Appendix A indicate that the use of polarimetric optimised phase does not guarantee the highest temporal coherence comparing to the single polarimetric channels (i.e. VV/VH). This implies that the numerical polarimetric optimization, which aim to optimize the a-priori selection criteria, does not necessarily result in improved real-world performance, at least for the dataset used in this work. Consequently, there is an opportunity to combine the TS-InSAR model parameters at post-PSC selection stage of the TS-InSAR analysis to increase MP density.

In an effect to further improve the performance of Pol-TS-InSAR, it may be possible to better utilise the multi-polarimetric data by considering the information from all polarimetric channels in addition to the polarimetric optimised data during the main TS-InSAR processing stage. Rather than treating the data from multiple polarisations as a single measurement with varies polarimetric characteristics and statistical properties, one could consider each polarimetric channels as an independent measurement, assuming that the scatterers within a resolution cells from different polarisation channels had a common or similar deformation signal. This assumption is adopted from the premise often employed in InSAR deformation analysis with Distributed Scatterers, wherein nearby pixels are assumed to belong to the same target or targets that exhibit the same deformation signal (Bamler and Hartl, 1998; Even and Schulz, 2018).

In this work, a few considerations have been made to adopt the main TS-InSAR processing stage with multi-polarimetric data: (1) for the minimal modification from the conventional TS-InSAR workflow, the modification should be stick to the processes relating only to the model parameters (i.e. deformation rate, DEM error, etc) estimation; (2) model parameters obtained from all polarimetric channels are combined using the weighted average computation, in which the estimated a-posteriori variance factor (Kampes, 2006) can be used as the weighting; (3) model parameters with temporal coherence (Ferretti et al., 2000, 2001) lower than a certain threshold (typically 0.75 depending on the number of images available) should be considered to be incorrect estimation and hence should not be included for the weighted average computation. The polarimetric optimised model parameters can be expressed as

$$\begin{aligned} h_{opt} &= \sum_k \frac{\omega_{pol_k}}{\sum_n \omega_{pol_n}} h_{pol_k} \\ d_{opt} &= \sum_k \frac{\omega_{pol_k}}{\sum_n \omega_{pol_n}} d_{pol_k} \end{aligned}, \quad \omega_{pol_k} = \begin{cases} 0, & \gamma_{pol_k} < \gamma_{threshold} \\ 1/\sigma_{pol_k}^2, & \gamma_{pol_k} \geq \gamma_{threshold} \end{cases} \quad (7)$$

where h_{opt} and d_{opt} are the optimised DEM error (difference) and deformation rate (difference), respectively; ω_{pol_k} is the inverse-variance weighting for polarisation channel k ; $\sigma_{pol_k}^2$ is the variance obtained from the temporal phase unwrapping process; γ_{pol_k} represents the temporal coherence of polarimetric channel number k , which the polarimetric channels used here include all single polarimetric channels and the polarimetric optimised channel; N is the number of polarisation channels. It is worth noting that polarimetric optimised channel used in this

approach is not limited to the ESPO method mentioned in section 2.1. Other polarimetric optimisation approaches such as CMD-Best (Zhao and Mallorqui, 2019), TM + TP (Shen et al., 2022) and PolPSI-ADI (Zhao et al., 2022), can be used to replace the method used to obtain the polarimetric optimised channel (see Appendix B in supplementary document for the performance of WS-MPMP with the optimised PSC from ESPO and TM + TP compared to the conventional method).

2.3. Overall pol-TS-InSAR processing framework

In this work, Pol-TS-InSAR analysis is conducted based on the GEOS-PSI approach (Ng et al., 2012b) to derive the deformation time-series from the multi-temporal DP S1 data, with the extension modules: (1) ESPO (Navarro-Sanchez et al., 2014) to increase the density and phase quality of the PS pixels; (2) integration of model parameters from multi-polarisation channels to increase the density of the MP and quality of the parameters estimated.

The single reference image approach is chosen (Ferretti et al., 2001), in which a single reference (primary) image is selected for the generation of interferogram stacks. The differential interferograms are generated using the InSAR Scientific Computing Environment (ISCE) software (Rosen et al., 2012) with two-pass differential InSAR approach (Massonnet et al., 1993). The one arc-second Shuttle Radar Topography Mission (SRTM) Digital Elevation Model (DEM) (Rodriguez et al., 2005) is used in the topographic phase removal process.

Once the differential interferogram stacks are generated, the ADI for every polarisation channels are computed based on Eq. (1). The multi-polarimetric ADI and their optimal phase values are then computed based on the ESPO method from section 2.1. All pixels with ADI lower than 0.4 are selected as PSC (PS candidates) for further analysis.

The high-quality PSCs, with ADI lower than 0.25, are first used to construct the reference network. The network is constructed based on Delaunay triangulation network. In addition, the maximum distance of connection between any two points was limited at 1.5 km to minimise the effect of atmospheric delay (Kampes and Nico, 2005). The displacement rate and DEM error for each arc in the reference network are computed using Least-Squares Ambiguity Decorrelation (LAMBDA), an integer least square method (ILS) (Kampes and Nico, 2005; Teunissen, 1995). This process is repeated for every polarimetric channels and the polarimetric optimised channel. WS-MPMP estimation, the model parameters estimation approach discussed in section 2.2, can hence be used to obtain the refined parameters, i.e., displacement rate and DEM error. The temporal coherence threshold ($\gamma_{\text{threshold}}$) of 0.75, corresponding to a noise variance of approximately 0.2 mm/yr derived from Colesanti et al. (2003)'s noise model, is used where estimations with value higher than the threshold can be assumed reliable. Therefore, if the temporal coherence of any polarisation channel at an arc is lower than the threshold, that particular channel at the arc will not be included for further analysis. In order to avoid the incorrect estimation from LAMBDA or inhomogeneous solutions between different polarisation channels, the spatial integration and outliers detection, based on M-Estimation (Tukey, 1977), is performed to estimate the displacement rate and DEM error for each point in the reference network. The parameters of the isolated PSCs, that are not included in the reference network, are estimated using the modified adaptive estimation strategy. The adaptive estimation strategy used in Ng et al. (2012b) is originally developed for single polarisation data. Therefore, instead of estimating the model parameters using single polarisation channel, it is necessary to estimate the parameters using multi-polarisation channels. The WS-MPMP estimation is hence adopted in the adaptive estimation strategy to deal with the multi-polarisation data. Any possible outliers MP are then removed using a quadtree filtering (Peng et al., 2022).

For this study, the reference point is chosen based on the continuous GPS (CGPS) data. The CGPS station near the metropolitan area (see Fig. 1a) that is stable in time is selected as the reference point. The TS-InSAR results are calibrated based on the selected CGPS station such that

the displacement data for each point is relative to the reference point. The atmospheric artefacts is corrected based on the approach used in Ng et al. (2012a), where both topography related and non-topography related atmospheric artefacts are estimated and corrected. In this work, elevation-related atmospheric signals and spatially correlated atmospheric turbulence signals are estimated separately. First, the elevation-related atmospheric signals are estimated based on the linear relationship between the MP's elevation and their unwrapped residual phase. The atmospheric turbulence signals are then estimated and corrected by a spatio-temporal filtering operation (Ferretti et al., 2001). A spatial low-pass filtering operation in with a window size of 400 m and a temporal high-pass filtering operation with a window size of 365 days is used for the filtering operation. It is worth to note that the unwrapped residual phase is obtained based on the weighted average of the unwrapped residual phase from all polarisation channels under the previously established network. The non-linear displacement component of each PS is then computed from the residual phase, the unwrapped phase after the modelled parameters and atmospheric artefacts are removed. Finally, the non-linear displacement component is combined with the linear counterpart to derive the displacement time series. In order to further suppress the decorrelation noise of the displacement time series, a temporal low pass filter with window size of 183 days is applied to improve the quality of the measurements with a trade-off of decrease in temporal resolution.

2.4. Validation and projection to vertical displacement with assistance of GPS data

In this work, the deformation results obtained by Pol-TS-InSAR analysis are compared with the CGPS measurement for validation. The InSAR-derived deformation is measured along the line of sight (LOS) direction of the radar. So, in order to assess the accuracy of deformation results obtained in this work, the GPS measured 3D displacements are projected into the LOS direction based on the parameters of the S1 satellite. The procedures used to match the deformation obtained from the two measurements mainly follow Ng et al. (2012a):

1. The measurement periods for all CGPS stations are assessed, only the stations with temporal overlap between GPS and InSAR measurement period that is more than 70% (~2 years) are selected for further analysis.
2. Since the reference point from the TS-InSAR analysis is selected with a reference GPS stations nearby, the displacement values in all other stations are adjusted with respect to reference GPS station.
3. For each GPS station, all MPs within 90 m of the station are selected to avoid the geolocation error.
4. The average of the selected MPs' displacement is computed for the InSAR-measured displacement at each GPS station for validation.
5. The difference between the InSAR- and GPS-measured displacements are computed for assessment.

Since the aim of this study is to apply the Pol-TS-InSAR for urban subsidence monitoring at Sydney area. Given that the groundwater extraction in the Botany Aquifer has been restricted, widespread groundwater subsidence is unlikely to occur (Ng et al., 2011). Therefore, it is assumed that the InSAR-derived deformation over the study area consists of two main deformation components: (1) the urban subsidence which is mainly in vertical direction and is relatively small in spatial extent; (2) continental plates movement which is mainly in horizontal direction, according to the CGPS data, and is large in spatial domain. The horizontal displacement in the InSAR result is expected to be dominated by the continental plates movement which can be removed prior to the subsidence analysis. Measurement from multiple viewing geometries are necessary to resolve the deformation in three dimensions (Pagli et al., 2014). Due to the lack of different viewing geometry, the GPS-measurement is used to remove the horizontal displacement in the

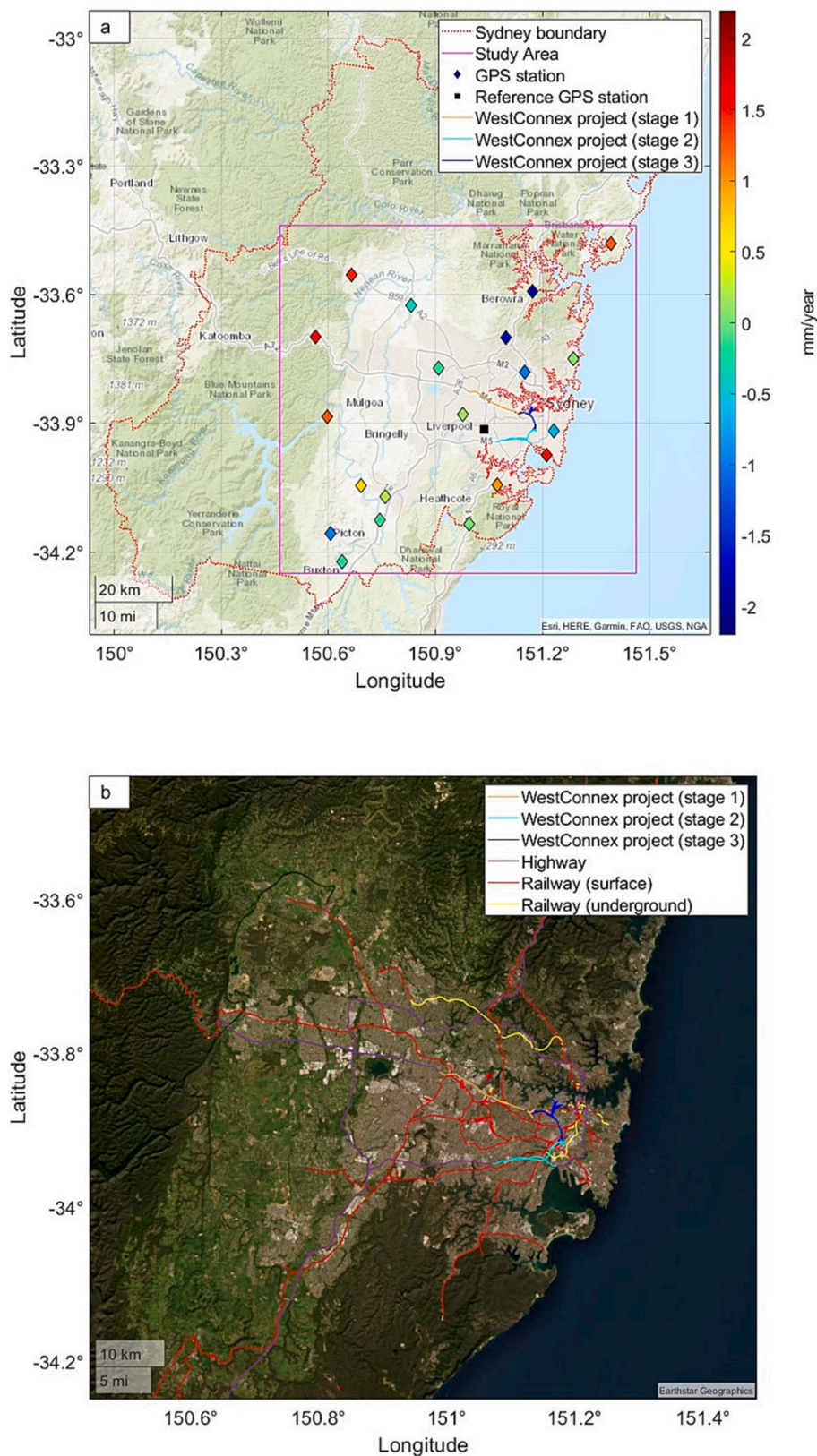


Fig. 1. (a) Topographic reference map for Greater Sydney region from Esri. The study area is highlighted by the magenta rectangle. The difference between GPS- and InSAR-measurements at each GPS stations used in this work is indicated by the square symbols. (b) Satellite optical image over the study area. (For interpretation of the references to colour in this figure legend, the reader is referred to the web version of this article.)

InSAR result. The GPS-measured easting and northing displacements are first projected into InSAR LOS direction. Then the 2nd order displacement trend is interpolated using the least square method. The horizontal displacement component is then subtracted from the LOS displacement of the InSAR result. The remaining LOS deformation can hence be assumed to be mainly consisting of the vertical displacement component and hence can be directly projected into the vertical direction.

3. Study area and dataset description

3.1. Study area

Sydney, the capital city of the state of New South Wales, is the most populous city in Australia with approximately 5.2 million residents (Fig. 1). The climate of Sydney is typically subtropical oceanic with warm summers (December to March) and mild winters (June to August). The average temperature ranges from 24 °C (peaked in January) to 13 °C (peaked in July). The rate of annual rainfall is fairly abundant at about 1175 mm. The rainfall rate is higher between January and June, with an average of about 705 mm. The wettest months are February and June. The rate is lower in the second half of the year, with an average of around 470 mm. Flooding is sometimes occurred in Sydney during the rainy period.

Being one of the most expensive cities in the world, the city is highly and densely urbanized. The Sydney area lies on shales and sandstones, which were deposited in Permian-Triassic Period (298 to 200 million years ago). The metropolitan area is relatively flat in south of the harbour. The region at the north of the harbour, with elevation rising to 200 m, consists of low rolling hills and wide valleys. To the west of the metropolitan region are hills and mountains, protected in some national parks. The agriculture is mainly concentrated in the region in the West.

The coverage of the area of interest, with an area of about 90 km × 90 km, covering most urban areas of Sydney is shown in Fig. 1. The building and transport infrastructures have been built extensively over the study area because of the urban development in recent years, for

example, the development of the 33 km WestConnex tunnels. WestConnex project is the largest transport project in Australia where the construction split up into three stages (Fig. 1). The construction for stage 1 (March 2015 – July 2019 with a depth of approximately 35 m below ground) and stage 2 (July 2015 – June 2020, with depth of up to 90 m below ground). The construction for stage 3, with depth of up to 55 m below ground commenced in 2019 and is expected to be completed in 2023. For the WestConnex project, several underground motorway interchanges have been constructed or approved for construction alongside with the tunnel's construction. Subsidence is often observed in the newly excavated tunnels and up-to-date information is important for detecting any possible potential risks related to the underground construction (Wu et al., 2017; Yan et al., 2021a).

3.2. InSAR dataset

Ninety C-band DP S1 IWS SAR images in TOPSAR mode (track 009), collected from 7 April 2019 to 22 March 2022, over the study area are analysed. The S1 images are acquired in descending orbits with spatial resolution of 5 × 20 m in range and azimuth, respectively. The primary image acquired on 10 October 2020 is chosen as the single reference image because the perpendicular and temporal baselines of the series of interferograms are relatively short with respect to this image (Fig. 2). Since the perpendicular baselines are well controlled in Sentinel-1, the image in the middle of the timespan is considered. The perpendicular baseline varies between 134 m and – 74 m and the time-period of observations spans 1080 days (approximately 3 years).

3.3. GPS dataset

The Asia-Pacific Reference Frame (APREF) solution is used in this work for cross-validation purpose. The broad objective of APREF is to create and maintain a densely realised and accurate geodetic framework in the Asia-Pacific region, based on continuous observation and analysis of GNSS data. APREF is currently composed of more than 1000 stations,

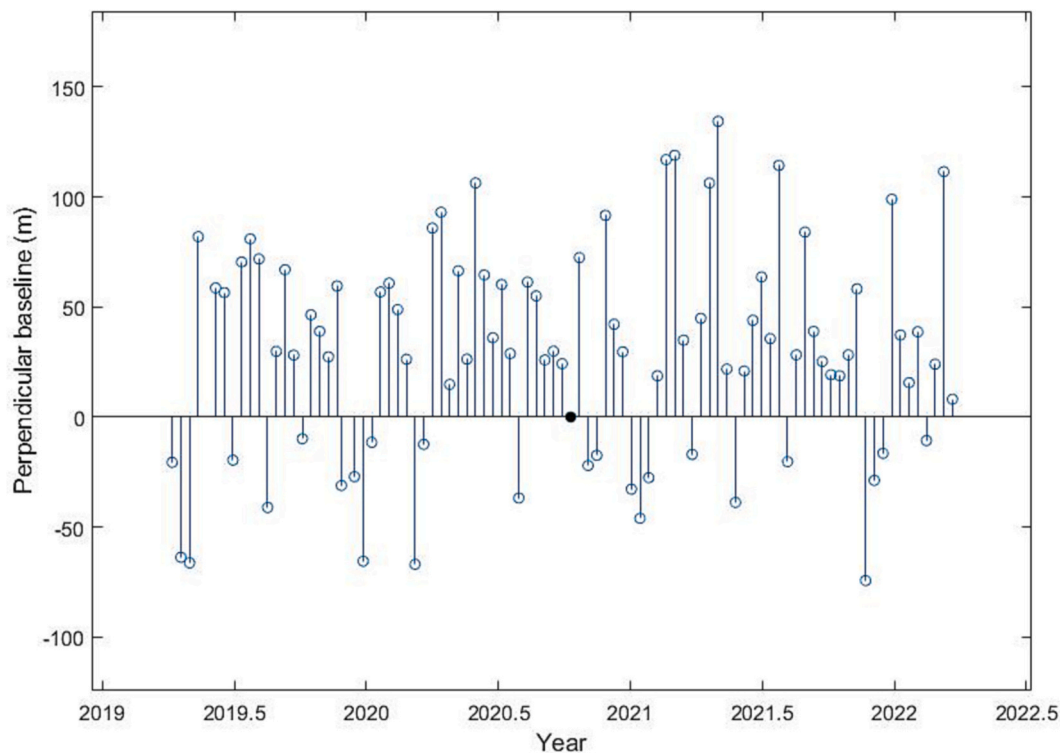


Fig. 2. Dual polarisation S1 dataset (Orbit direction: Descending; Imaging mode: IWS; Polarisation: VV/VH; Incidence angle: 30° ~ 41.2°; Look direction: Right). The black solid circle at zero perpendicular baseline represents the primary image (10 October 2020).

which are commonly operated by the national mapping agencies or private sector organisations. The data are collected in real time and transmitted through Internet to data centre in Geosciences Australia (GA) (<https://www.ga.gov.au/scientific-topics>).

The APREF solutions are analysed by four Local Analysis Centres (LACs) with the following state-of-the-art processing strategy: 1) use scientific software packages for the initial processing, e.g. Bernese, GAMIT, GIPSY; 2) conform to the IERS (International Earth Rotation Service) 2010 conventions and the IGS (International GNSS Service) guidelines, with the satellite orbits, clocks and the Earth orientation parameters fixed to the final IGS products; 3) contribute solutions in the SINEX format (Solution INdependent EXchange); 4) adopt IGS absolute antenna phase centre variation (PCV) calibration for satellites and receivers were used; and 5) finally the daily solutions are generated in SINEX format, and data cleaning has been done also by rejecting solutions with incorrect metadata. The weekly solution, which is aligned to the IGS08, is created by combining the daily final solutions with Bernese software on the daily normal equations level. The daily coordinate repeatability is 4–8 mm for the vertical component and 2–4 mm for the north & east horizontal components, respectively,

In this work, there are 35 stations found within the area of interest. However, three of them have no InSAR MP nearby (within 90 m) and only 22 have at least 2 years of temporal overlap with the InSAR measurements, i.e. 7 April 2019 to 22 March 2022. As a result, twenty-one stations, meeting both criteria, have been selected in this work (Fig. 1).

4. Results

4.1. Subsidence map and subsidence zone

The vertical displacement rate map generated from dual polarisation

S1 data at Sydney using the ESPO+WS-MPMP method is presented in Fig. 3 (see Fig. A4 in Appendix C in supplementary document for the results from other approaches). The reference point for the Pol-TS-InSAR analysis was chosen near the reference GPS station (Fig. 1a) due to its proximity to the Sydney Metropolitan area, providing a sufficient amount of MP nearby with relatively stable elevation to minimise the effect of mismatch in MP due to geolocation uncertainties. The ESPO+WS-MPMP, ESPO, VV, and VH approaches yielded approximately 5.90 million, 5.46 million, 3.28 million and 2.12 million MP, respectively, covering an area of approximately 6500 km². The corresponding average densities are approximately 903, 835, 502 and 325 points per km², respectively. Fig. 3 shows that the MP mainly distributed in the central part of the image, i.e., resident and business district. The density of MP is, however, gradually decrease as it goes further away from the metropolitan, i.e., western end as well as the north-south end of the displacement map. The land use in the north-south end of the displacement map is mainly the national parks which are covered by dense vegetation. The land use in western end is initially the agriculture area which becomes the mountainous area with density vegetation as it approaches the west end.

The displacement result suggests that Sydney was relatively stable in most area with the displacement rates at over 98% of the MP being between -4 mm/yr to 4 mm/yr across all approaches. The standard deviation of the displacement rate is between 1.3 and 1.5 mm/yr. The highest deformation rate observed is approximately -50 mm/yr. No regional scale land subsidence zones have been observed according to Fig. 3, although several small spatial scale subsidence areas have been observed. Five interesting subsidence zones are identified for further investigation: (A) the Sydney Central & Inner Metropolitan area, (B) Olympics park, (C) Jordan Springs East, (D) Spring Farm, (E) underground mine subsidence sites at the Southern Coalfield. The deformation

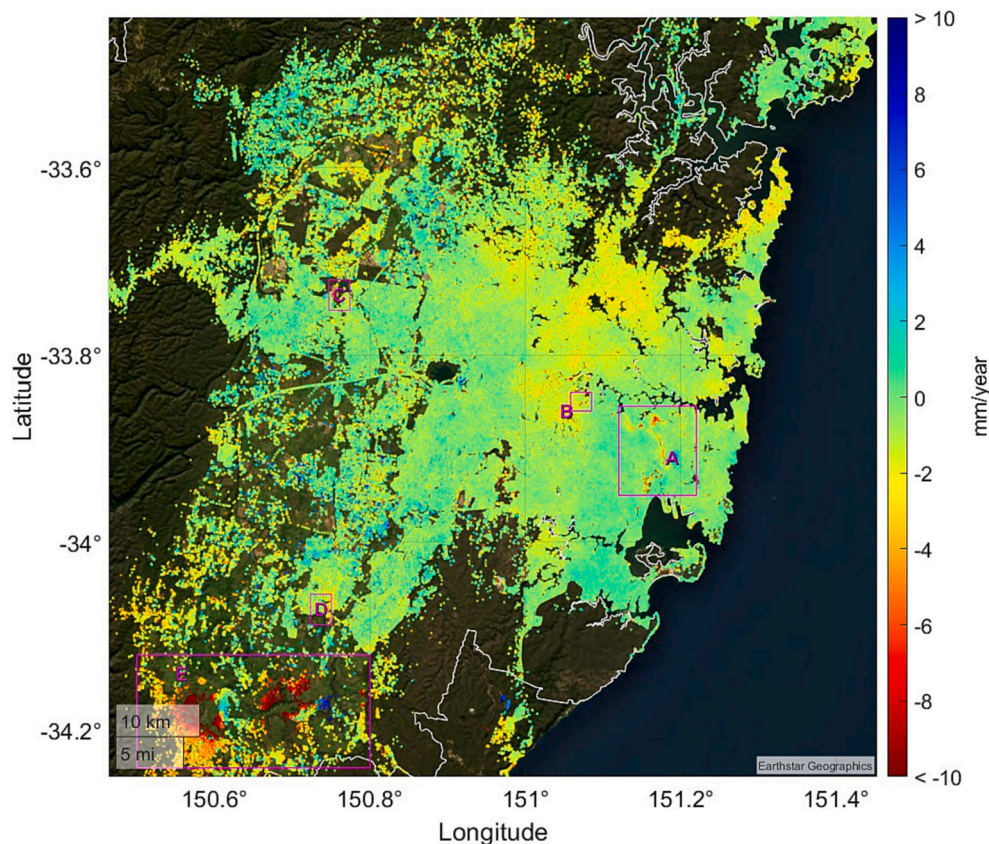


Fig. 3. Mean vertical displacement rate derived from Dual polarisation S1 data spanning 7 April 2019 to 22 March 2022. The five subsidence zones are highlighted by the purple boxes. (For interpretation of the references to colour in this figure legend, the reader is referred to the web version of this article.)

in Zone A is likely attributed to the WestConnex tunnel construction, Zones B, C, and D are suspected to be related to the historical landfill, and the subsidence in Zone E is induced by the underground coal mining. Further investigation of the subsidence phenomenon is discussed in the subsequent sections.

4.2. MP density obtained from different polarisation channels

The number of MPs obtained from the Pol-TS-InSAR is compared with the counterpart from the single polarisation TS-InSAR for further investigation. The comparison of number of MPs obtained from ESPO-WSMPMP, ESPO, VV and VH is conducted in two ways: (1) visual interpretation of the distribution of MPs near the deformation zone, (2) analysis of the densities of the MP at different land use types.

The vertical displacement rate maps generated from different approaches at the five subsidence zones are shown Appendix C in the supplementary document (Fig. A5 and A8 to A11). Analysis of the maps reveals that in Zone A, the density of MP obtained from ESPO+WS-MPMP and VV is slightly denser at the subsidence zone at the bottom right of Fig. A5, providing better insights into subsidence phenomena in that region. The profile plots in Fig. A6 shows that subsidence patterns for the three profiles agree each other in general, but some MPs are lacking for VH at the subsidence center in all three profiles. Additionally, there is a relatively large difference between the DP measurements and the SP (single polarisation) measurements near the subsidence centre in profile C-C'. This may be due to rapid deformation over the zones, where taking all MP within 90 m for each sample may smooth out the deformation signals, particularly for the DP measurements due to the denser MPs. For the case of Zone B (Fig. A9), the result from ESPO+WS-MPMP are apparently denser than other approaches at the rim of the extent of waste (highlighted by the blue arrows in Fig. A9). The same situation applies to Zone C (Fig. A8), where the MP obtained from the DP approaches are denser than those from the SP approaches. A comparison of the location of MP obtained from ESPO+WS-MSMS and ESPO is shown in Fig. A8f. It can be seen that there are more MP from ESPO+WS-MSMS, especially near the subsidence hot spot at the center of the map and the northern end of Jordan Spring East (highlighted by the white circles in Fig. A8f).

The density of MP obtained from different approaches at different land use types is shown in Table 1. In this study, the land use classification data GlobeLand30 (2020 version), the 30-m resolution global land cover data product developed by National Geomatics Centre of China (Jun et al., 2014), has been used. All MPs for each land use type within the study area are identified for comparison (see Fig. A12 in Appendix D in supplementary document for the classification map in Sydney). The result shows highest density of MP is observed from ESPO-WSMPMP for all land use types. The land use types with greatest improvement are forest, grassland, and near-shore Island and infrastructure (including the infrastructure along the lake shore).

Table 1
MP densities (point / km²) comparison of different approaches over different land use over Sydney.

Land-use type	ESPO + WS-MPMP		ESPO		VV		VH	
	PS	PSC	PS	PSC	PS	PSC	PS	PSC
Cultivated land	72.2	203.2	67.3	203.2	43.1	58.4	23.7	33.1
Forest	43.4	294.3	38.4	294.3	24.5	44.7	14.1	23.4
Grassland	215.7	455.8	195.6	455.8	128.1	166.0	75.8	97.8
Shrubland	363.2	568.6	349.4	568.6	215.1	247.3	167.0	183.4
Wetland	138.2	476.0	128.7	476.0	81.5	121.4	50.4	65.8
Artificial Surfaces	3213.5	4151.1	2979.9	4151.1	1782.3	2041.6	1160.9	1351.0
Bare Land	925.3	1293.4	852.5	1293.4	552.0	626.5	375.9	432.2
Near-shore Island and Infrastructure	90.4	244.2	82.1	244.2	52.9	71.1	33.7	42.7
Total	902.6	1323.4	835.4	1323.4	502.3	587.5	325.0	383.5

4.3. Validation with GPS data

The validation of the InSAR derived subsidence measurements of this work is conducted in two parts: (1) cross-validation between the results obtained from different approaches, and (2) comparison of the results and the measurements from the CGPS networks.

The overlaps MP between approaches are compared for cross-validation. The histograms and spatial distributions of the difference in measurements obtained from different approaches are shown in Fig. A13 of Appendix E in the supplementary document. The results indicate a good agreement among these measurements, with root mean square (RMS) difference ranging between 0.33 mm/yr and 1.07 mm/yr. It can be seen that the RMSE difference between ESPO+WS-MPMP and other approaches are lowest, with 0.33 mm/yr, 0.45 mm/yr and 0.56 mm/yr for ESPO, VV, and VH, respectively. The RMS difference of the VH measurements are largest comparing to other approaches, with 0.61 mm/yr and 1.07 mm/yr for ESPO and VV, respectively. As can be seen from the results, the proposed method exhibits an RMS difference of 0.45 mm/yr and 0.56 mm/yr compare to VV and VH, respectively. These values are lower than those observed in the ESPO, which yielded 0.50 mm/yr and 0.61 mm/yr, respectively, thereby suggesting a possibility of slight reduction in the noise from the proposed approach. It is observed from the spatial distributions of the difference that the regions with large RMS difference mostly appear at the southern end of the subsidence difference maps, especially at the mining area. It is possible due to the mixture of edging error and highly nonlinear subsidence phenomena, since this issue is mainly found in the area near the edge with sparse MP and rapidly deforming area with nonlinear characteristics, making it difficult to obtain the correct atmospheric phase screen and deformation estimation. This can be evidence in the VH measurements with lowest MP density with largest RMS difference.

The distribution between the GPS- and InSAR-measurements is shown in Fig. 4 and Table 2. Good agreement between both measurements has been observed with RMS difference of 0.95 mm/yr, 1.04 mm/yr, 0.95 mm/yr, and 1.02 mm/yr for ESPO+WS-MPMP, ESPO, VV, and VH, respectively. All stations are within the ± 2.4 mm/year range. It is worth to know that there are no nearby MP found in some of the GPS stations for VV and VH, therefore no comparison can be conducted at these stations for these channels. The InSAR- and GPS-derived subsidence time-series at the 21 GPS stations are shown in Figs. A14, A15, A16, and A17 corresponding to ESPO+WS-MPMP, ESPO, VV, and VH, in Appendix E in the supplementary document. The results show that the displacement trends agree each other in general, but some of the nonlinear displacement signals appear to be over-smoothed in the low-temporal resolution InSAR measurements.

5. Discussion

5.1. Performance assessment of the pol-TS-InSAR

5.1.1. Measurement point density

In order to evaluate the performance of ESPO+WS-MPMP for

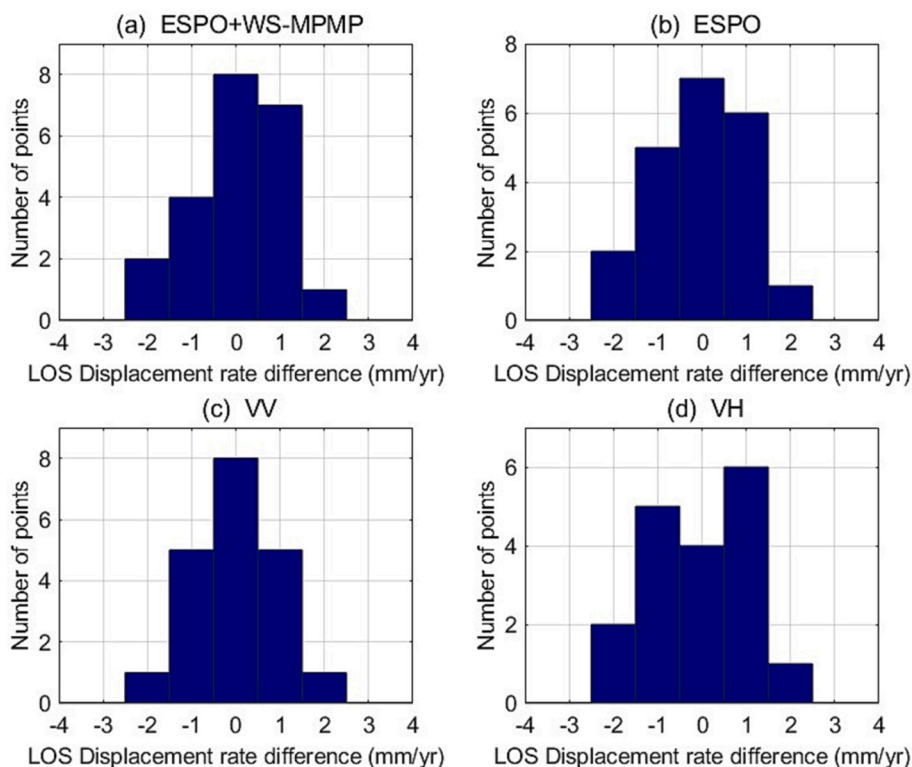


Fig. 4. Histogram of the difference between the GPS-measurements and the InSAR-measurements derived from (a) ESPO+WS-MPMP, (b) ESPO, (c) VV, and (d) VH. The red and green line indicate the mean and standard deviation of the difference between both measurements. (For interpretation of the references to colour in this figure legend, the reader is referred to the web version of this article.)

Table 2
The difference between the InSAR measurements and the GPS measurements.

(m)	ESPO+WS-MPMP	ESPO	VV	VH
RMS difference (mm/yr)	0.95	1.04	0.95	1.02
Absolute mean (mm/yr)	0.75	0.84	0.73	0.82
Highest difference (mm/yr)	2.14	2.16	2.40	2.02
Lowest difference (mm/yr)	-1.69	-1.84	-1.62	-2.01
No. of stations for comparison	21	21	20	18

deformation mapping, several aspects are analysed, including MP density, measurement accuracy, and computation time. Based on the comparison of MP density obtained from different approaches, the observed MP density is highest for ESPO+WS-MPMP, followed by ESPO, VV and finally VH. The result shows that the number of MP obtained by the DP approaches are much larger than the SP approaches, which is consistent with other Pol-TS-InSAR studies (e.g. Azadnejad et al., 2019; Navarro-Sanchez and Lopez-Sanchez, 2011; Navarro-Sanchez et al., 2014; Samsonov and Tiampo, 2011). An overall improvement of 8%, 80%, and 178% in MP density has been observed for ESPO+WS-MPMP compared to ESPO, VV and VH, respectively. The improvements of ESPO+WS-MPMP are particularly significant for the forest and grassland land-use types, with an increase of 13%, 78%, and 208% for forest, and 10%, 68%, and 184% for grassland when compared to ESPO, VV, and VH, respectively. The improvement can be attributed to the fact that the VV and VH may represent different scatterer centres over the vegetated area, which can deteriorate the deformation signals in the polarimetric optimised channel, obtained through combination of VV and VH signals. Consequently, the reliability of the deformation measurement derived from SP may be higher in these cases. The results suggest that ESPO+WS-MPMP, which considers deformation estimates from both polarimetric optimised channel and SP channels, has potential to yield more MP and accurate deformation measurements over these targets.

5.1.2. Measurement accuracy

Both cross-validation and validation with GPS measurements have been conducted to assess the measurement accuracy obtained from different approaches. The result of both validation indicates that the measurement accuracy of ESPO+WS-MPMP is numerically superior to other approaches. However, considering that the estimated measurement accuracies among all approaches are quite close, with differences smaller than the expected accuracy of the InSAR measurement, it is reasonable to conclude that the measurement accuracy obtained from all approaches in this work are approximately equivalent. One of the concerns arising from the DP approaches is the ratio of the final MPs and the PSCs, which is only 63% - 68%, significantly lower than that of the SP approaches (i.e. 85%-86%). Further investigation is necessary in the future to analyse whether the common threshold used for PSC selection remains efficient for the DP approach.

5.1.3. Computational time

In terms of processing time, the relative computation time of the other approaches is compared with that of the SP approach, which is used as the reference. The analysis was conducted on a processing server with dual sixteen-core Intel(R) Xeon(R) Gold 6226R processors (2.9 GHz) and 512 GB of RAM. During the interferogram stack generation stage, the DP approach required twice as much time as the SP approach using the ISCE software. However, this computation time can be significantly reduce to approximately 1.3 times with fine-tuning of the processing workflow, such as using the same terrain and co-registration parameters for all channels.

It is worth noting that time required for TS-InSAR analysis is dependent on the number of PSC selected. To enable consistent comparison, the relative computation time is determined by assuming the same number PSC are selected for processing. The computation time was longest for the ESPO+WS-MPMP approach, which required almost 2.3 times the ESPO processing time for the time-series analysis alone

(excluding the time to generate the interferogram stacks). The additional time required for ESPO+WS-MPMP approach was mainly due to the workload required to compute the model parameters, which were approximately three times greater than those required for the ESPO approach. Additionally, due to the heavy computation required to obtain polarimetric coefficients for polarimetric PSC selection, the processing time for the ESPO approach was approximately 1.9 times longer than the SP approach. A summary of the relative computation time between different approaches is shown in Table 3.

The applicability of ESPO+WS-MPMP may vary depending on different situations. User should evaluate whether the 8% improvement in MP density is worth almost threefold increase in processing time. Moreover, it is crucial to consider the available computational resources when deciding which approach to use. ESPO+WS-MPMP, and to some extent ESPO, demand significantly more computational power and storage space than the SP approaches, which may be a limiting factor for some users. Finally, it is also worth noting that the performance assessments of these approaches are based on the dataset used in this study. The performance of each approach may vary depending on the specific dataset being analysed. Further investigation is necessary, i.e. applying these approaches on multiple datasets and full polarisation channels, is necessary for drawing a more reliable conclusion.

5.2. Interpretation of subsidence areas in Sydney

5.2.1. Land deformation caused by tunnel construction

A detailed investigation of the subsidence zone A in Fig. 3 is conducted. The displacement rate map along the WestConnex tunnel (stage 3) alignment is shown in Fig. 6 and Fig. A5. Based on the visual interpretation from Fig. 6, it can be seen that the subsidence pattern matches well with the location of the third stage of the WestConnex project (construction commenced in 2019). The maximum subsidence observed is approximately 10 mm/yr along the tunnel and 15 mm/yr near the tunnel interchange. The mean vertical displacement rate with respect to the distance from the tunnel centre of the WestConnex tunnel construction stage 3 is computed (Fig. 5). The result suggested that the subsidence rate increases as the tunnel centre is approached, which is a typical characteristics of the land settlement induced by tunnel excavation (Macchiarulo et al., 2021; Yan et al., 2021b). Similar subsidence patterns cannot be observed for stage 1 of WestConnex and can only be partially observed for stage 2 of WestConnex, mainly near St Peters Interchange. The possible reasons are: (1) almost all construction works for stage 1 were completed before the acquisition period, (2) most of the construction works for stage 2 were completed before 2017 except the area near the St Peters Interchange, which is expected to be completed in 2024. This suggested most land settlement has stabilised shortly after construction was completed, except the areas near the interchange.

The subsidence profile lines A-A', B-B' and C-C' from Fig. 6 are shown in Fig. 7 and Fig. A6. The profile line A-A' crosses over the Rozelle Interchange which consists of many tunnels (Fig. 7a). It can be seen that there are two subsidence peaks, which are within the two tunnels regions. The profile lines B-B' and C-C' shows the displacement cross-sections at the Pymont Bridge Road section of the stage 3 WestConnex project. It is worth noting that although similar subsidence patterns have been observed from the two profile lines, the dates of excavation are differed for the two profiles. Fig. 8 (a) and (b) shows the subsidence time-series of the MP near the peak subsidence of profile B-B' and C-C', respectively. In order to understand the relationship between

land subsidence and the progress of tunnel excavation, the time-evolution of the land surface is compared with the excavation period. According to work notification reports from the WestConnex official web site (<https://www.westconnex.com.au/>), the excavation work for MPs in Fig. 8 (a) and (b) began in early October 2020 and June 2020, respectively. The excavation works completion dates were in early February 2020 and January 2021 for the two MPs, respectively. Since the tunnelling location in the work notification reports only show the approximate location and progress of the tunnelling activities, the excavation periods have been expanded by one month before and after the reported dates to avoid mis-location issues. Both time-series results in Fig. 8 (a) and (b) show that the subsidence rates during the excavation periods are between 25 and 30 mm/year, which is much higher than the subsidence rates at the pre- and post-excavation period. Both results show that the land became stabilised shortly after the completion of excavation. However, higher subsidence rate has been observed for the MP at Profile B-B' (11 mm/yr) compared to the MP at Profile C-C' (4 mm/yr) in the pre-excavation period. One of the possible reasons was the land is affected by the tunnelling work of the temporary access tunnel, which was being constructed along the transverse direction of the WestConnex tunnel since May 2019. Another reason was the pre-construction observation period in Profile C-C' is much longer than Profile B-B', so the impact of the nearby excavation is less domination when the subsidence rate is computed.

5.2.2. Possible land deformation related groundwater levels

Variation in groundwater levels is one of the common factors that lead to land deformation in urban areas. In fact, groundwater subsidence within the Botany Aquifer has already been reported in previous literatures (e.g. Ng et al., 2008), which will not be discussed in this work. This works will focus on two deformation phenomena observed from InSAR results: the area near Cooks River and Bardwell Valley ('o' symbol in Fig. 6) and the northern end of the Alexandra canal ('Δ' symbol in Fig. 6).

It is worth noting that stage 2 of WestConnex tunnels mainly run through sandstone and shale rock. However, there is a proportion of the tunnels which dive deep into the paleochannel, filled with soft alluvium, near the Cooks River and Bardwell Valley (near Sydney Airport). This area is hence subject to subsidence especially when underground construction operations have taken place. In fact, ongoing inflow of groundwater into the tunnels near this area has been reported during both excavation and operation. Subsidence has been observed mostly in the alluvium plains near the Cooks River and Bardwell Valley with a peak rate of over 10 mm/yr. In order to deal with the groundwater inflow issue, a water treatment plant has been built to treat the groundwater and discharge approximately 2ML of groundwater per day, into the Cooks River. Fig. 8c shows the subsidence time-series at the water treatment plant in the area. Continued subsidence has been observed with a rate of 10.8 mm/yr even after the tunnel construction. Therefore, this settlement is suspected to be related to the groundwater drawdown. However, since the location is also near several tunnel entries and exits, there is a possibility that soil consolidation has been a contributing factor to the settlement, as the soils are more likely to be compressible over this region.

A relatively large uplift zone has been found with a rate of 9.9 mm/yr which is centred near 'Δ' symbol in Fig. 6. This is an interesting phenomenon because no deformation phenomenon was expected at the location at least in the 2010s to the authors' knowledge. The uplift zone is located near the northern end of the Alexandra canal ('Δ' symbol in Fig. 6) within the Botany Aquifer. The Botany Aquifer is the largest aquifer in Sydney, where the rainwater seeps into the northern end of the sandy aquifer and flows into the sea at the southern end at a speed of approximately 150 m/year. The water levels in Alexandra Canal, one of the groundwater discharges in the Botany Aquifer, controls the groundwater flows. The groundwater passes beneath the uplift zone to Alexandra Canal before discharging to surface waters. To further

Table 3

Relative cost time comparison between difference approaches (computation time of the SP approach is used as the reference).

	SP (VV or VH)	ESPO	ESPO+WS-MPMP
Interferogram stack generation	1	~1.33	~1.33
TS-InSAR analysis	1	~2.40	~6.24

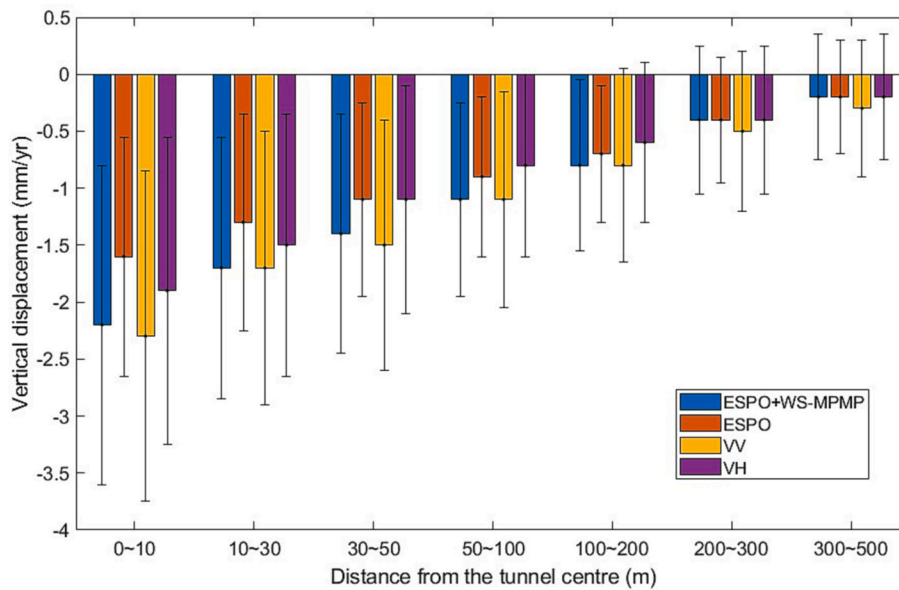


Fig. 5. The relationship between the mean vertical displacement rate and the distance from the tunnel centre of WestConnex tunnel construction stage 3.

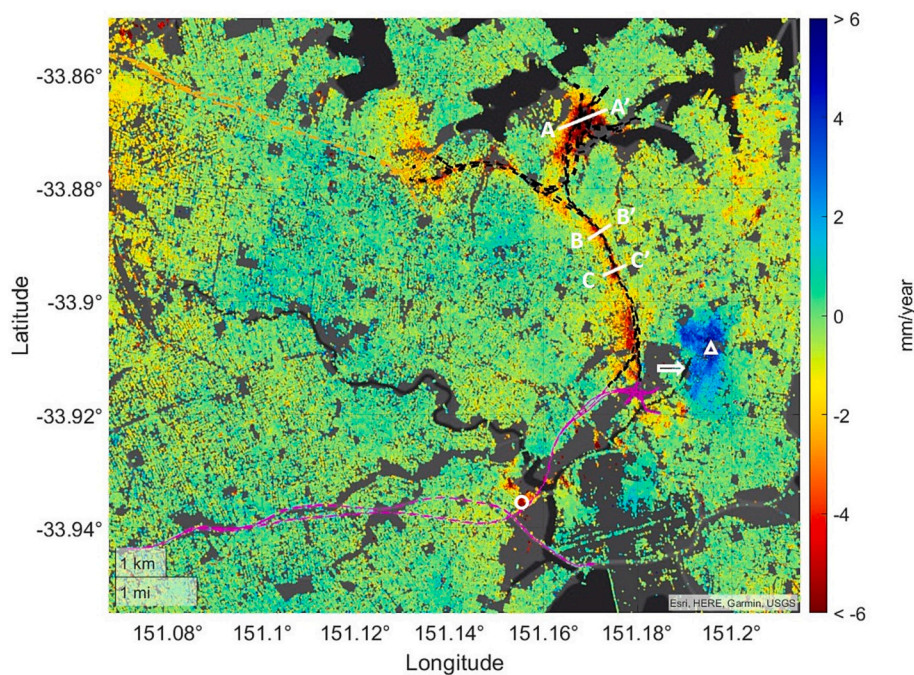


Fig. 6. The vertical displacement rate map for zone A in Fig. 3. The orange, purple, and black broken lines highlight the WestConnex tunnels alignment for stage 1, 2 and 3, respectively. The white lines indicate the locate of profile lines A-A', B-B' and C-C'. The white arrow indicates the northern end of the Alexandra canal. (For interpretation of the references to colour in this figure legend, the reader is referred to the web version of this article.)

investigate the possible reasons for this phenomenon, the deformation time series near the centre of the uplift zone (Fig. 8d) is investigated. It can be seen that the land has been subsiding at a rate of 2.1 mm/yr until early 2020 and has become uplifting with a rate of 8.1 mm/yr since then. There maybe three possible reasons for this phenomenon: (1) the construction work of the WestConnex project near the Alexandra Canal, which includes two new road bridges built across the canal between 2016 and 2020 (opened in June 2020), partial deconstruction and reconstruction of the canal wall, and new stormwater discharge outlets built to discharge stormwater to the canal, could influence the water levels in Alexandra Canal and hence affect the groundwater flows from the aquifer to the canal; (2) the extraction of groundwater over the uplift

area has been further restricted since February 2018 according to the “Temporary Water Restrictions Order for the Botany Sands Groundwater Source 2018”. No groundwater extraction is expected near the area except any possible dewatering for WestConnex related construction after 2018, and hence leading to an increase in groundwater level; (3) combined effect of the first and second reasons.

5.2.3. Land deformation in the landfill area

Jordan Spring East (JSE, Zones C in Fig. 3) is a new residential development in Llandilo, near Penrith in Sydney’s west, which has been recently reported with land subsidence incidents observed (Maddison, 2020). More than 800 houses in the suburb are identified by the city

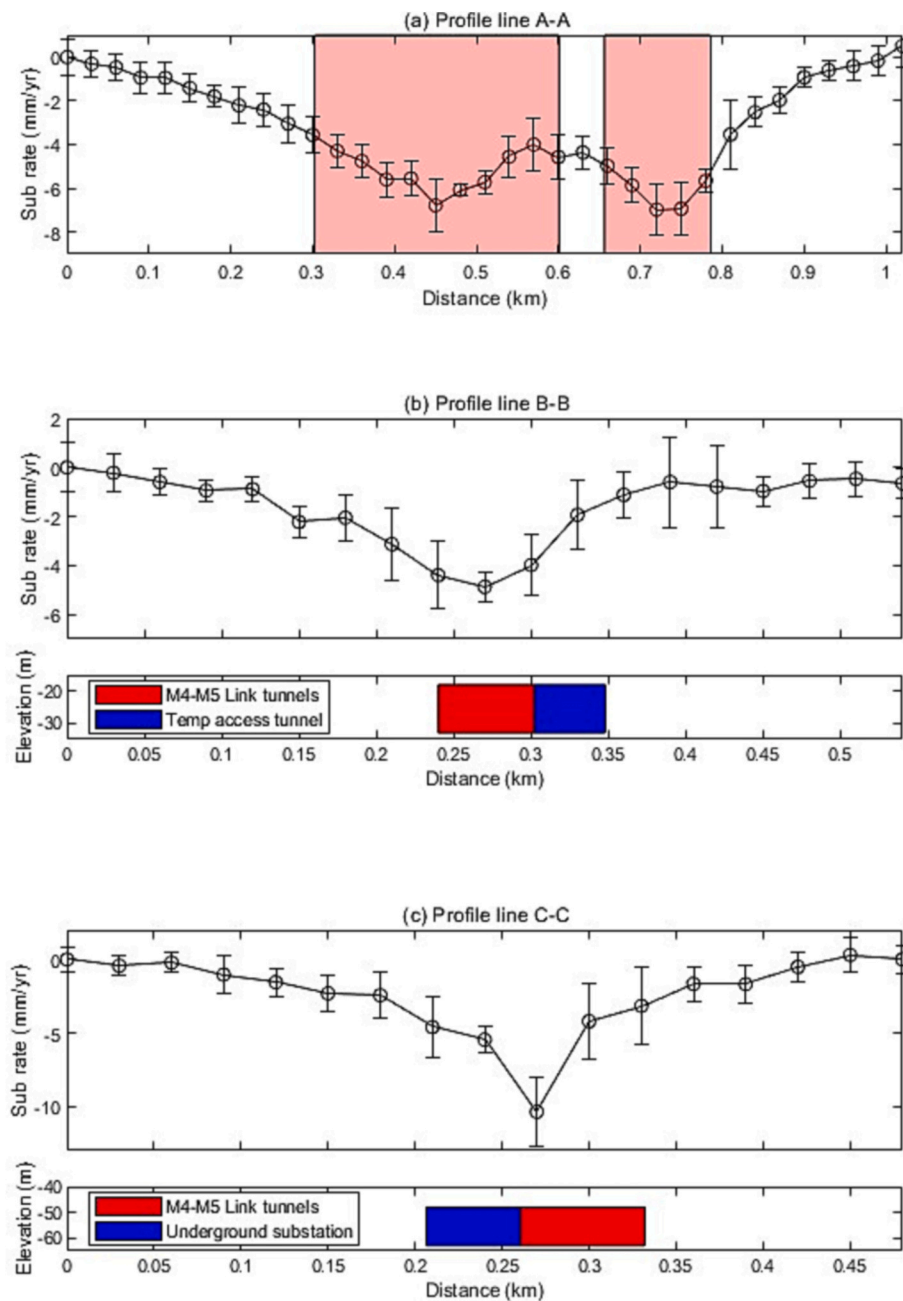


Fig. 7. Profile plots for profile lines (a) A-A', (b) B-B' and (c) C-C' in Fig. 6. The location of the tunnels at the Rozelle Interchange are highlighted by red. (For interpretation of the references to colour in this figure legend, the reader is referred to the web version of this article.)

council as being at risk, and a number of houses were reported to have been demolished because of the excessive ground deformation. The vertical displacement rate maps for the JSE are shown in Fig. 9 and Fig. A8. Fig. 9b reveals that land subsidence condition in JSE can be separated into two parts, with land subsidence rate over 20 mm/yr observed in the eastern side of JSE, while the western side shows relatively stable land with a slight uplift. In fact, JSE is underlain by Triassic Bringelly Shale (west), and Pleistocene to Tertiary alluvial sediments (east) (Constandopoulos et al., 2009). A comparison of the land subsidence map with the geological map shows that the subsidence pattern matches well with the geological units. The Luddenham soil layer is developed on Triassic Bringelly Shale, which is found on gently undulating rises on the shale terrains. On the other hand, the subsidence areas are mainly located on the alluvial floodplain deposits, where the land over the region is filled with soil and other materials to reclaim the land

for development. Khalili and Mitchell (2020) demonstrates that at least a section of the fill platform contains uncontrolled earthworks including insufficiently compacted landfill, therefore it is expected that the land subsidence observed in JSE is related to the landfill operation. To further investigate the relationship between the land subsidence and the landfill operation, the average depth of fill at the 6 test sites in Khalili and Mitchell (2020) are analysed. Fig. 9c shows the distribution of the land subsidence rates against the depth of the fill materials. A clear correlation of -0.56 has been observed between the observations, suggesting the magnitude of the land subsidence is related to the depth of the fill in JSE. However, since the number of samples used for the comparison is limited, further investigation in the future is necessary to support the relationship obtained when more ground survey data is available.

Other historical landfill sites have also been found to be experiencing land subsidence, e.g., the Sydney Olympic Park (SOP) remediation area

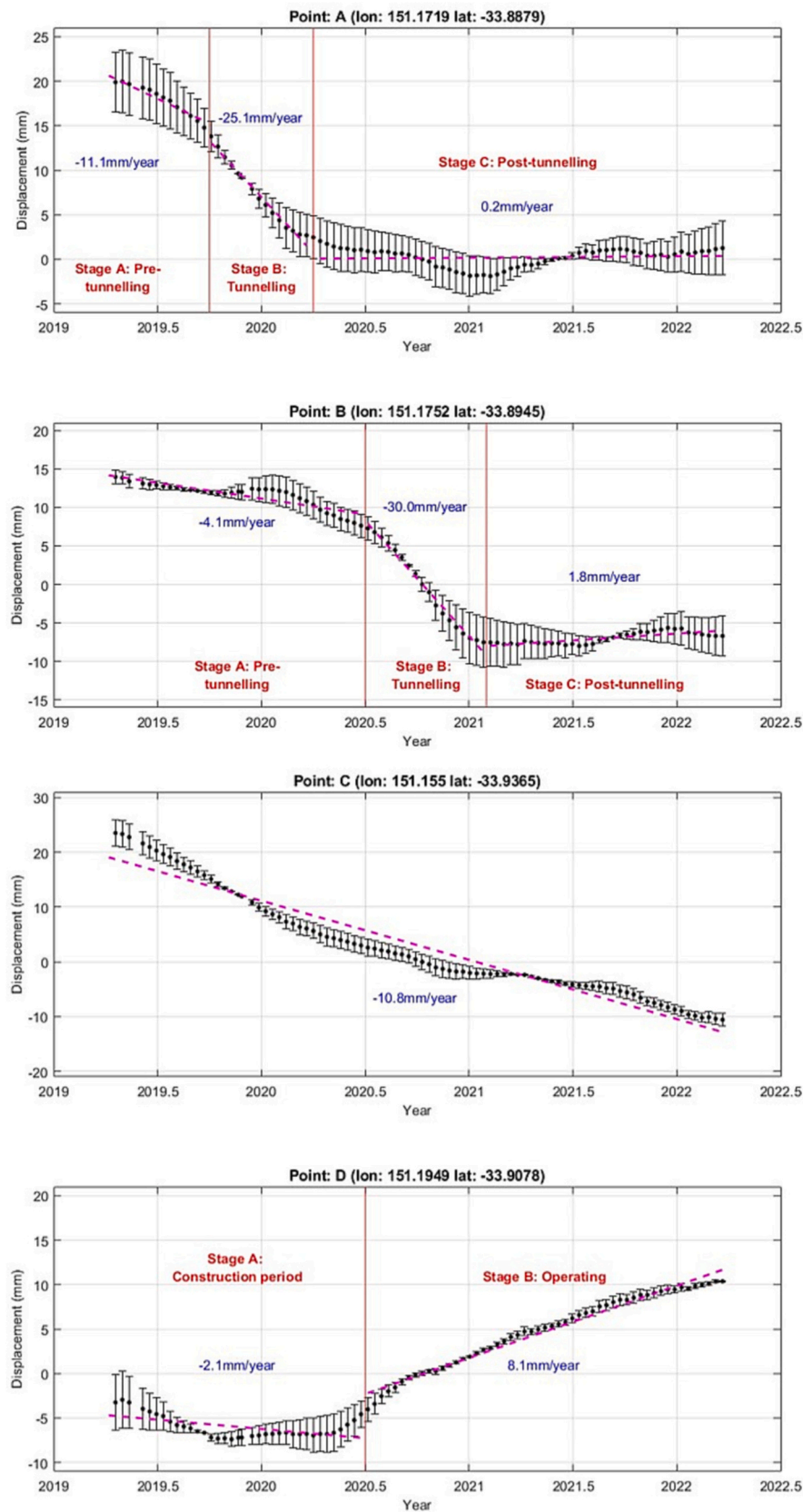


Fig. 8. InSAR-measured displacement series at MPs near the centre of (a) profile B-B' and (b) profile C-C' in Fig. 6; (c) water treatment plant near Cooks River (highlight by 'o' in Fig. 6); (d) uplift zone near Alexandra canal entrance (highlight by 'Δ' in Fig. 6). The error bars are calculated based on the displacement standard deviation from the nearby MPs. See Fig. A7 for the deformation times-series from all approaches.

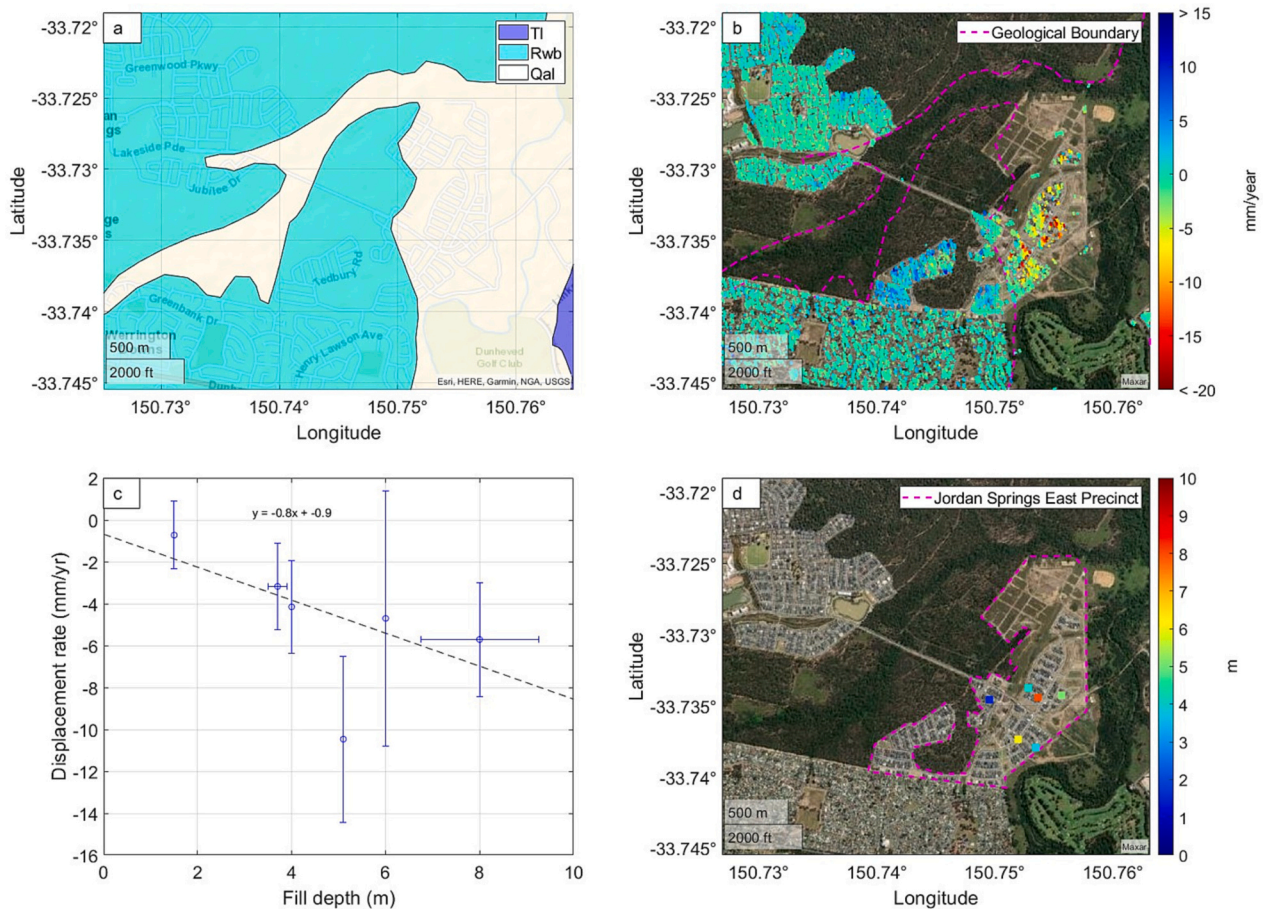


Fig. 9. (a) The geological and (b) the vertical displacement rate maps at Jordan Spring East (Zone C in Fig. 3). The geological units in (a) includes Londonderry Clay (T1), Bringelly Shale (Rwb), Alluvial floodplain deposits (Qal) (adopted from the Penrith 1:100,000 geological map). (c) The relationship of the fill depth and the subsidence rate. (d) The location of the sample points for the analysis between fill depth and subsidence rate.

and the western Spring Farm. The remediation of old waste sites at SOP was, at that time, the largest-ever landfill remediation project in Australia. There was excessive landfilling of domestic, commercial, and industrial waste in the past, which required some form of remediation before it was transformed into the residential and commercial land-use in the early 2000s. The boundary of some of the historical waste landfill sites in SOP is shown in Fig. 10a and Fig. A9, where the area is known to have land filling with both waste and other fill materials. Fig. 10a shows that the density of MP in the vegetated area in the landfill sites is limited. However, almost all MPs with high subsidence rate are still observed within the boundaries of the sites with a subsidence rate of over 12 mm/yr. Some deforming MPs with subsidence rate of approximately 5 mm/yr are observed outside the landfill sites. These MPs are mostly located at the sites of recently developed high-rise building. Therefore, the land deformation at these MPs is likely to be related to heavy loading and the construction of the infrastructures.

Fig. 10b and Fig. A10 show the land displacement maps at the western part of Spring Farm, where landfill operations were conducted before the land-use was transformed from industrial and mining land-use into residential land-use. Two large subsidence bowls were found adjacent to each other along the Springs Road in Fig. 10b, with peak subsidence rate of over 15 mm/yr. According to Willis (2010), these areas were used for the dumping and treatment of night soil in the past with extensive sand mining nearby. One of the possible reasons for the formation of subsidence bowls is possibly because of land in these regions was not filled and compacted properly, i.e., uncontrolled fill.

5.2.4. Land deformation caused by mine subsidence

The Southern Coalfield, located at the southern part of the Sydney Basin, is one of the 5 major coalfields in the state of New South Wales (NSW). Fig. 11 and Fig. A11 show the vertical displacement velocity maps over the Appin and Tahmoor Collieries, the two most active coal collieries in the Southern Coalfield. Almost all coal mines in the Southern Coalfield are underground coal mines where longwall mining technique is employed. The land subsidence induced by longwall mining technique is often highly non-linear in time with a large deformation gradient. This spatio-temporal subsidence characteristic together with the strong temporal decorrelation over the vegetation implies that C-band S1 data is not suitable to map deformation over the site (Ng et al., 2017), especially using the linear displacement model during the TS-InSAR analysis. This problem can be seen in the subsidence velocity map (Fig. 11), where the density of MPs is limited over the site, especially over the center of the longwalls. Even though the MPs are sparse over the center of the longwalls, subsidence can be clearly seen at the rim of the longwall panels, with peak subsidence rate of over 40 mm/yr. The subsidence rate observed from TS-InSAR results may be underestimated since the phase ambiguity may not be solved correctly with the linear deformation model used. However, it is possible to claim that the land subsidence over this site is caused by mining activities based on the current information available. Further investigation can be conducted in the future to obtain the precise land subsidence information, e.g. other data such as a mine subsidence model can be used to complement the InSAR technique to avoid the phase unwrapping problems (Dai et al., 2021; Yang et al., 2018; Yang et al., 2017).

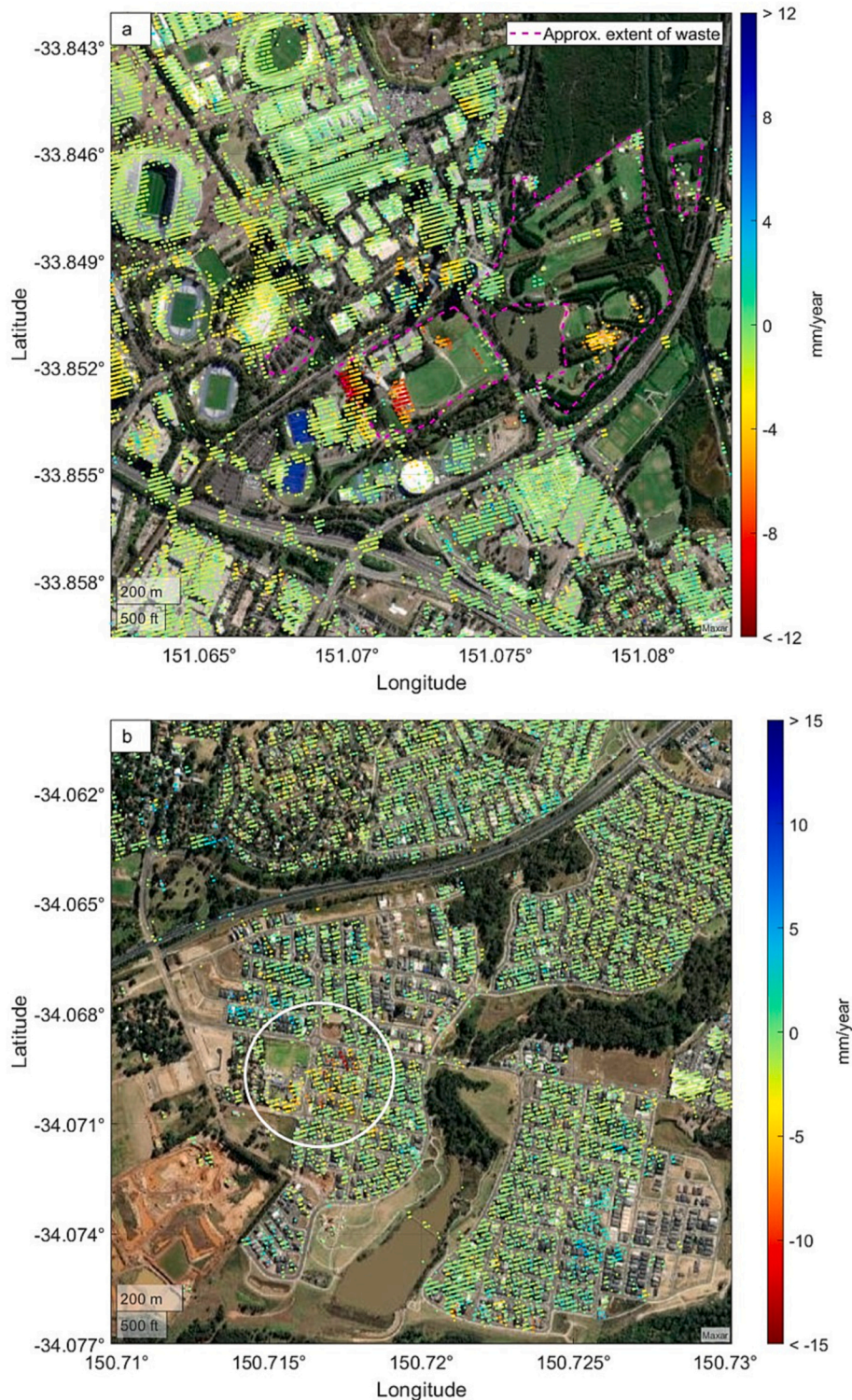


Fig. 10. The vertical displacement rate maps at (a) Sydney Olympic Park remediation area (Zone B in Fig. 3) and (b) western Spring Farm (Zone D in Fig. 3). The rapid subsidence zone in Spring Farm is highlighted by the white cycle.

5.2.5. Evolution of subsidence phenomenon in from 1990s to 2020s

The subsidence measurements obtained in this study are compared with previous works focusing on Sydney. In general, the caused and location of the subsidence phenomenon in Sydney have evolved over time, with the exception of the mine subsidence in the Southern coalfield.

Groundwater subsidence was one of the dominant subsidence factors in 1990s, as evidenced by the regional scale subsidence in the Eastern

Suburb (Ng et al., 2008). However, the scale of groundwater subsidence has substantially decreased since 2000s, according to Ng et al. (2011), who reported no regional scale groundwater subsidence was observed. The InSAR results from present study is consistent with Ng et al. (2011), suggesting that the groundwater subsidence is likely well controlled in Sydney. The reduction in regional scale groundwater subsidence can likely attributed to the restriction imposed on groundwater extraction in Botany Aquifer in 2006 and further restrictions in 2018. It is important

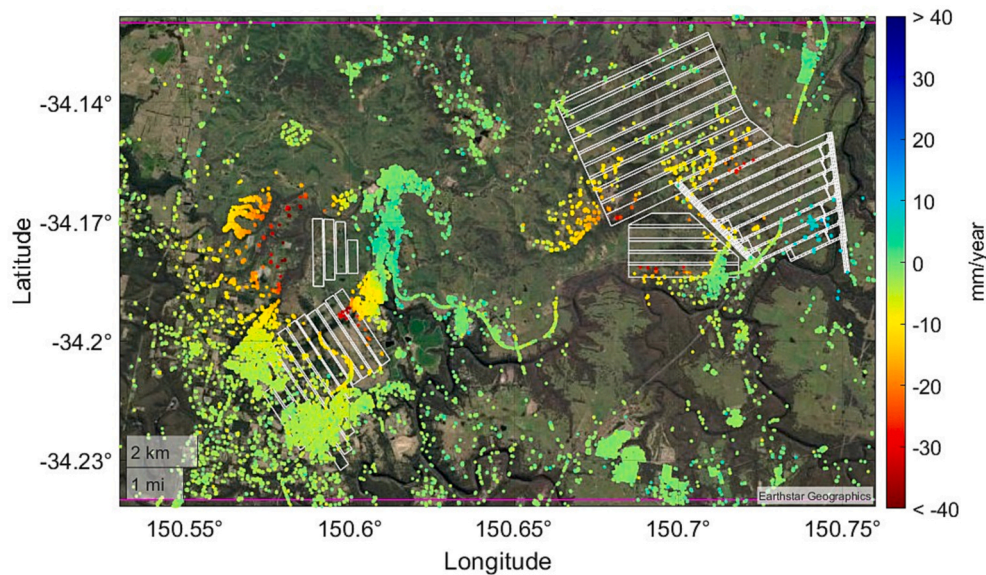


Fig. 11. The vertical displacement rate maps at Appin and Tahmoor Collieries (Zone C in Fig. 3). The white lines represent the longwalls in these collieries.

to note that local scale groundwater-related subsidence are still occurs in Sydney, for example in the vicinity of Botany Bay, Cooks River and Bardwell Valley.

In the context of tunnel excavation-induced subsidence, Bateman et al. (2020) conducted a study on land subsidence resulting from Sydney's metro tunnel construction using both the TerraSAR-X and ENVI-SAT imagery. Their findings suggested that the ground deformation from tunnelling could be assumed as negligible because of Sydney's geology. However, in this study, the subsidence along the WestConnex tunnels have been observed. This subsidence phenomena is not observed from the 2020s subsidence maps (Ng et al., 2011), i.e. before the construction work started, suggesting the subsidence observed is mostly like related to the tunnel construction work for the WestConnex project, indicating that the impact of tunnel excavation on ground deformation may not be generally negligible in all cases.

Owing to rapid urban expansion, land subsidence in the urban development areas has become an increasing concern in recent years (Stewart, 2019). The urban development related subsidence incidents in Sydney are often reported in the reclamation areas and the historical landfill zones, which is consistent with the findings of this study. Several subsidence zones observed in this work are associated with landfill areas. This suggests that the land stability of all landfill areas in Sydney region should be carefully monitor and understand before, during and after development processes.

Land subsidence resulting from underground mining in the Southern Coalfield has already been reported in several previous studies (Du et al., 2018; Falorni et al., 2018; Ge et al., 2008; Ng et al., 2017). It has been observed that the location of the subsidence centres varies between studies, because of the progress of the mining activities, such as advancement of coal face. Furthermore, the magnitude of the peak subsidence observed in this results is considerably lower than that reported in earlier studies. This inconsistency can be attributed to the scarcity of MP at near the centre of the subsidence bowls, as PS-based time-series analysis alone is not the optimal monitoring tool for mapping underground mine subsidence (Ng et al., 2010).

6. Conclusion

In this study, a novel Pol-TS-InSAR processing strategy is developed to enhance the utilisation of multi-polarisation data in the TS-InSAR process chain. This strategy considers the multi-polarisation data as separate measurements and assigns different weights to each

polarisation channel at each MP for TS-InSAR analysis. The developed Pol-TS-InSAR processing strategy is applied to map the land deformation in Sydney, Australia using 90 DP S1 images acquired between April 2019 and 22 March 2022. The results obtained from the developed approach is compared to the results obtained from the single polarisation approach as well as the conventional Pol-TS-InSAR approach (i.e. ESPO). An increased in MP density has been observed in the ESPO+WS-MPMP result compared to the single polarisation results (68% ~ 208%) and the ESPO results (4%–13%) across various land use types. In order to assess the precision of the results obtained from the new strategy, the Pol-TS-InSAR measurements have been compared to the GPS measurements. An absolute mean difference of 0.75 mm/yr and RMS difference of 0.95 mm/yr were observed at 21 CGPS stations, which is comparable to accuracy obtained from other approaches.

The land stability in the study area, with area of approximately 6500 km², has been investigated based on the 5,898,683 MPs (903 MP per km²) obtained from Pol-TS-InSAR analysis. In addition to the already-known groundwater subsidence and mine subsidence, this study reveals that the underground tunnel construction and potential improper landfilling are significant contributing factors to land subsidence in Sydney.

A clear relationship between land subsidence and the construction of the WestConnex tunnel has been observed in Sydney's Central & Inner Metropolitan area. Subsidence phenomena have been identified in Olympics Park, Jordan Springs East and Spring Farm, which are located at historical landfill sites. A clear correlation between the fill depth and subsidence rate is evident in Jordan Springs East, suggesting that the areas with inappropriate landfill is vulnerable to land subsidence. Furthermore, subsidence incidents have been noted at high-rise building construction sites, with a slightly lower magnitude to other subsidence factors. Among all subsidence factors observed in Sydney, the magnitude of ground surface subsidence appears to be largest in mine subsidence. However, mine sites in Sydney are commonly located in the rural areas and the mine-induced subsidence are often well monitored.

Despite the lower magnitude of subsidence from other factors such as underground tunnel construction and improper landfilling, these occurrences are often found in developed residential and business zones containing buildings and infrastructures. If not adequately monitored and managed, these subsidence events could lead to substantial economic losses and pose threats to human safety.

CRedit authorship contribution statement

Alex Hay-Man Ng: Conceptualization, Methodology, Software, Investigation, Visualization, Formal analysis, Writing – original draft, Writing – review & editing, Supervision. **Ziyue Liu:** Visualization, Formal analysis, Investigation, Validation. **Zheyuan Du:** Methodology, Investigation, Resources, Validation, Writing – review & editing, Supervision, Project administration. **Hengwei Huang:** Software, Formal analysis. **Hua Wang:** Conceptualization, Methodology, Investigation, Writing – review & editing. **Linlin Ge:** Investigation, Supervision, Writing – review & editing.

Declaration of Competing Interest

The authors declare that they have no known competing financial interests or personal relationships that could have appeared to influence the work reported in this paper.

Data availability

Data will be made available on request.

Acknowledgments

The authors thank ESA for providing the Sentinel-1A/B data. This research was funded by the Program for Guangdong Introducing Innovative and Entrepreneurial Teams (grant number 2019ZT08L213), National Natural Science Foundation of China (grant number 42274016), and Natural Science Foundation of Guangdong Province (grant number 2021A1515011483).

Appendix A. Supplementary data

Supplementary data to this article can be found online at <https://doi.org/10.1016/j.rse.2023.113694>.

References

- Azadnejad, S., Maghsoudi, Y., Perissin, D., 2019. Investigating the effect of the physical scattering mechanism of the dual-polarization sentinel-1 data on the temporal coherence optimization results. *Int. J. Remote Sens.* 40, 7033–7047.
- Azadnejad, S., Maghsoudi, Y., Perissin, D., 2020. Evaluation of polarimetric capabilities of dual polarized Sentinel-1 and TerraSAR-X data to improve the PSInSAR algorithm using amplitude dispersion index optimization. *Int. J. Appl. Earth Obs. Geoinf.* 84, 101950.
- Bamler, R., Hartl, P., 1998. Synthetic aperture radar interferometry. *Inverse Probl.* 14, R1–R54.
- Bateman, G., McCormack, H., Holley, R., Thomas, A., Och, D., 2020. The use of satellite Technology on Sydney Metro Northwest tunnel construction.
- Cloude, S.R., 2010. *Polarisation: Applications in remote sensing*. Oxford University Press, Oxford, U.K.
- Cloude, S.R., Papathanassiou, K.P., 1998. Polarimetric SAR interferometry. *IEEE Trans. Geosci. Remote Sens.* 36, 1551–1565.
- Colesanti, C., Ferretti, A., Novali, F., Prati, C., Rocca, F., 2003. SAR monitoring of progressive and seasonal ground deformation using the permanent scatterers technique. *IEEE Trans. Geosci. Remote Sens.* 41, 1685–1701.
- Constandopoulos, J., D'Angola, E., Smith, A., McNally, G., Hossain, A., Burns, A., Parra, G., 2009. St Mary's project central precinct plan: water, soils and infrastructure report. In: Sinclair Knight Merz, p. (p. 98).
- Dai, Y., Ng, A.H.M., Wang, H., Li, L., Ge, L., Tao, T., 2021. Modeling-assisted InSAR phase-unwrapping method for mapping mine subsidence. *IEEE Geosci. Remote Sens. Lett.* 18, 1059–1063.
- Du, Z., Ge, L., Ng, A.H.-M., Li, X., 2018. Investigation on mining subsidence over appin-west cliff colliery using time-series SAR interferometry. *Int. J. Remote Sens.* 39, 1528–1547.
- Dzurisin, D., 2007. *Volcano deformation: New geodetic monitoring techniques*. Praxis Publishing Limited, Chichester, UK.
- Esmaceli, M., Motagh, M., Hooper, A., 2017. Application of dual-polarimetry SAR images in multitemporal InSAR processing. *IEEE Geosci. Remote Sens. Lett.* 14, 1489–1493.
- Even, M., Schulz, K., 2018. InSAR deformation analysis with distributed scatterers: a review complemented by new advances. *Remote Sens.* 10, 744.
- Falorni, G., Del Conte, S., Bellotti, F., Colombo, D., 2018. InSAR monitoring of subsidence induced by underground mining operations. In: *Caving 2018: Proceedings of the Fourth International Symposium on Block and Sublevel Caving*. Australian Centre for Geomechanics, pp. 705–712.
- Ferretti, A., Prati, C., Rocca, F., 2000. Nonlinear subsidence rate estimation using permanent scatterers in differential SAR interferometry. *IEEE Trans. Geosci. Remote Sens.* 38, 2202–2212.
- Ferretti, A., Prati, C., Rocca, F., 2001. Permanent scatterers in SAR interferometry. *IEEE Trans. Geosci. Remote Sens.* 39, 8–20.
- Ge, L., Chang, H.C., Ng, A.H.M., Rizos, C., 2008. Spaceborne radar interferometry for mine subsidence monitoring in Australia. In: *First International Future Mining Conference and Exhibition 2008*, Proceedings, pp. 119–124.
- Herrera-García, G., Ezquerro, P., Tomás, R., Béjar-Pizarro, M., López-Vinielles, J., Rossi, M., Mateos, R.M., Carreón-Freyre, D., Lambert, J., Teatini, P., Cabral-Cano, E., Erkens, G., Galloway, D., Hung, W.-C., Kakar, N., Sneed, M., Tosi, L., Wang, H., Ye, S., 2021. Mapping the global threat of land subsidence. *Science* 371, 34–36.
- Ishitsuka, K., Matsuoka, T., Tamura, M., 2017. Persistent scatterer selection incorporating polarimetric SAR interferograms based on maximum likelihood theory. *IEEE Trans. Geosci. Remote Sens.* 55, 38–50.
- Ishitsuka, K., Tamura, M., Matsuoka, T., 2014. Equivalent stacking of polarimetric synthetic aperture radar interferograms based on analysis of persistent and distributed scatterers. *IEEE Geosci. Remote Sens. Lett.* 11, 1360–1364.
- Jun, C., Ban, Y., Li, S., 2014. Open access to earth land-cover map. *Nature* 514, 434.
- Kampes, B., Nico, A., 2005. The STUN algorithm for persistent scatterer interferometry. In: *Ouwelhand, L., Lacoste, H. (Eds.), Proceedings of the FRINGE Workshop 2005*, p. 16.11. Frascatti, Italy.
- Kampes, B.M., 2006. *Radar interferometry: Persistent scatterer technique*, 1st ed. Springer, Dordrecht, Netherland.
- Khalili, N., Mitchell, P.W., 2020. Jordan Springs east (JSE) joint report. In: *LN Engineering Consulting Pty. Ltd., Sydney, Australia*, p. (p. 23)..
- Liu, Z., Ng, A.H.-M., Wang, H., Chen, J., Du, Z., Ge, L., 2023. Land subsidence modeling and assessment in the West Pearl River Delta from combined InSAR time series, land use and geological data. *Int. J. Appl. Earth Obs. Geoinf.* 118, 103228.
- Macchiariulo, V., Milillo, P., DeJong, M.J., González Martí, J., Sánchez, J., Giardina, G., 2021. Integrated InSAR monitoring and structural assessment of tunnelling-induced building deformations. *Struct. Control. Health Monit.* 28, e2781.
- Maddison, M., 2020. Sydney's sinking suburb Jordan Springs east to get a \$600m bailout. In: *The Australian*. The Australian, Sydney.
- Massonnet, D., Rossi, M., Carmona, C., Adragna, F., Peltzer, G., Feigl, K., Rabaute, T., 1993. The displacement field of the landers earthquake mapped by radar interferometry. *Nature* 364, 138–142.
- Navarro-Sanchez, V.D., Lopez-Sanchez, J.M., 2011. On the selection criteria for pixel candidates in (PSI): potentials of polarimetry. In: *Proceedings of the 4th TerraSAR-X Science Team Meeting*. DLR, Wessling, Germany.
- Navarro-Sanchez, V.D., Lopez-Sanchez, J.M., Ferro-Famil, L., 2014. Polarimetric approaches for persistent scatterers interferometry. *IEEE Trans. Geosci. Remote Sens.* 52, 1667–1676.
- Navarro-Sanchez, V.D., Lopez-Sanchez, J.M., Vicente-Guijalba, F., 2010. A contribution of polarimetry to satellite differential SAR interferometry: increasing the number of pixel candidates. *IEEE Geosci. Remote Sens. Lett.* 7, 276–280.
- Ng, A.H.-M., Chang, H.C., Zhang, K., Ge, L., Rizos, C., 2008. Land subsidence monitoring in Australia and China using satellite interferometry. In: *Sideris, M.G. (Ed.), Observing our Changing Earth*. Springer, Berlin Heidelberg, pp. 743–750.
- Ng, A.H.-M., Ge, L., Du, Z., Wang, S., Ma, C., 2017. Satellite radar interferometry for monitoring subsidence induced by longwall mining activity using Radarsat-2, Sentinel-1 and ALOS-2 data. *Int. J. Appl. Earth Obs. Geoinf.* 61, 92–103.
- Ng, A.H.-M., Ge, L., Li, X., Abidin, H.Z., Andreas, H., Zhang, K., 2012a. Mapping land subsidence in the Jakarta city, Indonesia using persistent scatterer interferometry (PSI) technique with ALOS PALSAR. *Int. J. Appl. Earth Obs. Geoinf.* 18, 232–242.
- Ng, A.H.-M., Ge, L., Li, X., Zhang, K., 2012b. Monitoring ground deformation in Beijing, China with persistent scatterer SAR interferometry. *J. Geod.* 86, 375–392.
- Ng, A.H.-M., Ge, L., Zhang, K., Li, X., 2011. Application of persistent scatterer interferometry for land subsidence monitoring in Sydney, Australia using ENVISAT ASAR data. In: *34th International Symposium on Remote Sensing of Environment*. Sydney, Australia.
- Ng, A.H.M., Ge, L.L., Yan, Y.G., Li, X.J., Chang, H.C., Zhang, K., Rizos, C., 2010. Mapping accumulated mine subsidence using small stack of SAR differential interferograms in the southern coalfield of New South Wales, Australia. *Eng. Geol.* 115, 1–15.
- Onuma, T., Ohkawa, S., 2009. Detection of surface deformation related with CO₂ injection by DInSAR at in salah, Algeria. *Energy Proc.* 1, 2177–2184.
- Pagli, C., Wang, H., Wright, T.J., Calais, E., Lewi, E., 2014. Current plate boundary deformation of the Afar rift from a 3-D velocity field inversion of InSAR and GPS. *J. Geophys. Res. Solid Earth* 119, 8562–8575.
- Peng, L., Wang, H., Ng, A.H.-M., Yang, X., 2022. SAR offset tracking based on feature points. *Front. Earth Sci.* 9 <https://doi.org/10.3389/feart.2021.724965>.
- Perissin, D., Ferretti, A., 2007. Urban-target recognition by means of repeated spaceborne SAR images. *IEEE Trans. Geosci. Remote Sens.* 45, 4043–4058.
- Pipia, L., Fabregas, X., Aguasca, A., Lopez-Martinez, C., Duque, S., Mallorqui, J.J., Marturia, J., 2009. Polarimetric differential SAR interferometry: first results with ground-based measurements. *IEEE Geosci. Remote Sens. Lett.* 6, 167–171.
- Rodriguez, E., Morris, C.S., Belz, J.E., Chapin, E.C., Martin, J.M., Daffer, W., Hensley, S., 2005. An assessment of the SRTM topographic products. In: *Report No. JPL D-31639*. In: *Jet Propulsion Laboratory, Pasadena, California, USA*.
- Rosen, P.A., Gurrrola, E., Sacco, G.F., Zebker, H., 2012. The InSAR scientific computing environment. In: *EUSAR 2012; 9th European Conference on Synthetic Aperture Radar*, pp. 730–733.

- Rucci, A., Ferretti, A., Guarnieri, A.M., Rocca, F., 2012. Sentinel 1 SAR interferometry applications: the outlook for sub millimeter measurements. *Remote Sens. Environ.* 120, 156–163.
- Sadeghi, Z., Zoj, M.J.V., Hooper, A., Lopez-Sanchez, J.M., 2018. A new polarimetric persistent scatterer interferometry method using temporal coherence optimization. *IEEE Trans. Geosci. Remote Sens.* 56, 6547–6555.
- Samsonov, S., Tiampo, K., 2011. Polarization phase difference analysis for selection of persistent scatterers in SAR interferometry. *IEEE Geosci. Remote Sens. Lett.* 8, 331–335.
- Shamshiri, R., Nahavandchi, H., Motagh, M., 2018. Persistent scatterer analysis using dual-polarization Sentinel-1 data: contribution from VH Channel. *IEEE J. Sel. Top. Appl. Earth Obs. Remote Sens.* 11, 3105–3112.
- Shen, P., Wang, C., Lu, L., Luo, X., Hu, J., Fu, H., Zhu, J., 2022. A novel polarimetric PSI method using trace moment-based statistical properties and Total power interferogram construction. *IEEE Trans. Geosci. Remote Sens.* 60, 1–15.
- Stewart, S., 2019. Mascot towers might be sinking, according to engineers' report. In: ABC News. ABC News, Australia.
- Teunissen, P.J.G., 1995. The least-squares ambiguity decorrelation adjustment: a method for fast GPS integer ambiguity estimation. *J. Geod.* 70, 65–68.
- Tukey, J.W., 1977. *Exploratory data analysis*. Addison-Wesley, Reading, USA.
- Willis, I., 2010. Spring Farm, Yesterday and Tomorrow. *Macarthur Mag.* 10 (14), 54–58. Sydney South West Graphics.
- Wu, H.-N., Shen, S.-L., Yang, J., 2017. Identification of tunnel settlement caused by land subsidence in soft deposit of Shanghai. *J. Perform. Constr. Facil.* 31, 04017092.
- Yan, J., Liu, X., Bai, X., Zhang, M., Jiao, Y., Jing, D., Liu, H., Wang, Z., Kang, W., 2021a. Research on surface subsidence of long-span underground tunnel. *Adv. Civil Eng.* 2021, 6643892.
- Yan, Y., Yang, Q., Jia, Z., Zhang, X., Dai, H., Ng, A.H.-M., 2021b. Integration of multiband InSAR and leveling measurements for analyzing the surface subsidence of shield tunneling at Beijing-Zhangzhou high-speed railway. *J. Sens.* 2021, 6640077.
- Yang, Z., Li, Z., Zhu, J., Feng, G., Wang, Q., Hu, J., Wang, C., 2018. Deriving time-series three-dimensional displacements of mining areas from a single-geometry InSAR dataset. *J. Geod.* 92, 529–544.
- Yang, Z., Li, Z., Zhu, J., Yi, H., Hu, J., Feng, G., 2017. Deriving dynamic subsidence of coal mining areas using InSAR and logistic model. *Remote Sens.* 9, 125.
- Zhang, K., Song, R., Wang, H., Wu, D., Wang, H., 2016. Interferometric phase reconstruction using simplified coherence network. *ISPRS J. Photogramm. Remote Sens.* 119, 1–9.
- Zhao, F., Mallorqui, J.J., 2019. Coherency Matrix Decomposition-Based Polarimetric Persistent Scatterer Interferometry. *IEEE Trans. Geosci. Remote Sens.* 57 (10), 7819–7831.
- Zhao, F., Wang, T., Zhang, L., Feng, H., Yan, S., Fan, H., Xu, D., Wang, Y., 2022. Polarimetric persistent scatterer interferometry for ground deformation monitoring with VV-VH Sentinel-1 data. *Remote Sens.* 14, 309.